Divergence-conforming discretization for Stokes problem on locally refined meshes using LR B-splines

Kjetil André Johannessen, Mukesh Kumar and Trond Kvamsdal
Department of Mathematical Sciences
Norwegian University of Science and Technology, Trondheim, Norway.
E-mail: Kjetil.Johannessen@math.ntnu.no, Mukesh.Kumar@math.ntnu.no and Trond.Kvamsdal@math.ntnu.no

Abstract

To solve the incompressible flow problems using isogeometric analysis, the div-compatible spline spaces were originally introduced by Buffa [10, 11], and later developed by Evans [20]. In this paper, we extend the div-compatible spline spaces with local refinement capability using Locally Refined (LR) B-splines over rectangular domains. We argue that the spline spaces generated on locally refined meshes will satisfy compatibility provided they span the entire function spaces as governed by Mourrains [29] dimension formula. We will in this work use the *structured* refined LR B-splines as introduced by Johannessen *et al.* [25]. Further, we consider these div-compatible LR B-spline spaces to approximate the velocity and pressure fields in mixed discretization for Stokes problem and a set of standard benchmark tests are performed to show the stability, efficiency and the conservation properties of the discrete velocity fields in adaptive isogeometric analysis.

1 Introduction

Isogeometric analysis (IGA) was introduced in [23] as an innovative numerical methodology for the discretization of Partial Differential Equations (PDEs). The main idea was to improve the interoperability between Computer Aided Design (CAD) and PDE solvers, and to achieve this, the authors in [23] proposed to use CAD mathematical primitives, i.e. splines and NURBS, to also represent PDE unknowns. The smoothness of splines is a new ingredient that yields several advantages: for example, it improves the accuracy per degree of freedom and allows for the direct approximation of higher order PDEs. Isogeometric methods have been used and tested on a variety of problems of engineering interests, for flow simulations [2, 4, 7, 10, 14, 20, 17, 18], and for electromagnetic problems [12, 13, 32].

In electromagnetic and incompressible fluids flow simulations, numerical discretizations have to preserve the geometric structure of underlying PDEs in order to avoid spurious behaviors, instability or non-physical solution. Thus the numerical discretizations have to be related through a discrete De Rham complex. Compatible spaces for finite element approximations were in general introduced by Arnold *et al.* [3], and more recently in isogeometric analysis context, by Buffa *et al.* [10, 11]. High regularity of splines is advantageous for constructing compatible spaces. Some initial work to show the potential impact of compatible spline based methodology for electromagnetic wave computations was presented in [12, 32] and recently using T-spline complexes in [13]. The first isogeometric discretizations of incompressible fluid flows was done by Bazilevs *et al.* [6], generalizing Taylor-Hood elements to NURBS. Later, Buffa *et al.* [10] investigated a solver based on three choices of discrete spline spaces to approximate the mixed discretization for Stokes problem, which were seen as a smooth extension of Taylor-Hood (TH), Nedelec (N) and Raviart-Thomas (RT) pair of Finite Element (FE) spaces. One of their main finding was the smooth RT pair of spline based FE spaces provides divergence-free discrete solutions. Later using the idea of div-compatible spline spaces presented in the setting of discrete differential forms [11], a series of isogeometric divergence conforming spline discretizations were derived to solve Stokes and Brinkman equations, steady and unsteady Navier-Stokes equations by Evans in [17, 18, 19]. These initial developments show that isogeometric analysis is a highly accurate and efficient methodology to solve incompressible flow problems. In this paper our aim is extend the div-comptaible spaces to locally refined meshes and explore the benefit of adaptive refinement in solving incompressible flow problems. Adaptivity and local refinement allows us to not only achieve optimal convergence by resolving strong singularities, it also allows us to resolve local behaviour such as recirculation eddies in fluid flow. While the framework presented here is formulated on an unmapped rectangular domain, it is conjectured that it

is possible to extend it to mapped geometries using the Piola mapping in the same way as [10].

Non-uniform rational B-splines (NURBS) is the dominant geometric representation format for CAD. The construction of NURBS are based on a tensor product structure and, as a consequence, knot insertion is a global operation. To remedy this a local refinement can be achieved by breaking the global tensor product structure of multivariate splines and NURBS. Several techniques have been proposed to address this, among others are T-splines [36, 35], Hierarchical B-splines [21, 26], Truncated Hierarchical B-splines [22] and Locally Refined (LR) B-splines [15]. While initially, most of the references address the problem from a CAD point of view, later years have seen them applied to isogeometric analysis. For T-splines consider [5, 16, 33, 37, 38], for Hierarchical B-splines consider [30, 39, 8, 34], and for LR-splines see [25, 27].

1.1 Aim and outline of the paper

The aim of this paper is to present a class of compatible spline spaces with local refinement capability which form a De Rham complex and provide a stable, divergence-free discretization of the 2D Stokes problem.

The paper is organized as follows:

We start in Section 2 with our model Stokes problem which can be seen as a prototype of viscous incompressible flows. The necessary conditions to derive a divergence conforming spline discretization and the main results of the paper are presented.

In Section 3, we introduce the basic concepts of splines over locally refined Box-meshes (or T-meshes). We present the dimension formula as given by Mourrain [29] which will be useful in proving the compatibility among the splines spaces on locally refined meshes. Further we discuss the construction of derivatives spaces on locally refined meshes.

In Section 4, we present three different complete De Rham complexes on locally refined meshes. The complexes are characterized by their boundary conditions for the velocity space: (i) without boundary conditions, (ii) with no penetration boundary conditions, and (iii) with no slip boundary conditions.

To build a basis on the Box meshes we introduce the locally refined (LR) B-splines in Section 5. We give a brief overview of their generality before defining a subclass which we will use for the local refinement. This is the structured mesh refinement as introduced in [25].

In Section 6, we present some numerical results for Stokes problems. The numerical stability, convergence rates, efficiency and conservation properties of the proposed LR B-spline discretization in adaptive isogeometric analysis will be main focus.

Finally, some conclusions and perspectives are included in Section 7.

2 Stokes problem and Divergence-conforming spline discretization

To model a viscous incompressible flow, we consider the following Stokes problem: find $(\mathbf{u}, p)$ such that

$$\left\{ \begin{array}{rcl} -\nu\nabla^2\mathbf{u} + \nabla p &=& \mathbf{f} \text{ in } \Omega \\ \nabla\cdot\mathbf{u} &=& 0 \text{ in } \Omega \end{array} \right. \tag{1}$$

with suitable boundary conditions and a constant viscosity term ν. We consider $\mathbf{f} \in \mathbf{L}^2(\Omega)$ and $\Omega \subset \mathbb{R}^2$ is a rectangular domain.

We considered the mixed variational form of (1); find $\mathbf{u} \in \mathbf{H}^1(\Omega)$ and $p \in L^2(\Omega)$ such that

$$\left\{ \begin{array}{rcll} a(\mathbf{u},\mathbf{v}) + b(\mathbf{v},p) &=& f(\mathbf{v}) & \forall \mathbf{v} \in \mathbf{H}^1(\Omega) \\ b(\mathbf{u},q) &=& 0 & \forall q \in L^2(\Omega) \end{array} \right. \tag{2}$$

where

$$a(\mathbf{u},\mathbf{v}) = \int_\Omega \nu\nabla\mathbf{u} : \nabla\mathbf{v}$$

$$b(\mathbf{v},q) = -\int_\Omega q \text{ div } \mathbf{v} \quad \text{and} \quad f(\mathbf{v}) = \int_\Omega \mathbf{f}\cdot\mathbf{v}.$$

The discrete mixed form of (2) is obtain by solving the problem: find $\mathbf{u}_h \in V_h \subset \mathbf{H}^1(\Omega)$ and $p_h \in Q_h \subset L^2(\Omega)$ such that

$$\left\{ \begin{array}{rcll} a(\mathbf{u}_h,\mathbf{v}_h) + b(\mathbf{v}_h,p_h) &=& f(\mathbf{v}_h) & \forall \mathbf{v}_h \in V_h \\ b(\mathbf{u}_h,q_h) &=& 0 & \forall q_h \in Q_h, \end{array} \right. \tag{3}$$

where V_h and Q_h are finite dimensional subspaces.

In order to guarantee the stability, we consider the choices of discrete pair of approximation spaces $\{V_h, Q_h\}$ which satisfy the *inf-sup stability* conditions, i.e.,

$$\inf_{\substack{q_h\in Q_h \\ q_h\neq 0}} \sup_{\substack{\mathbf{v}_h\in V_h \\ \mathbf{v}_h\neq 0}} \frac{b(\mathbf{v}_h, q_h)}{\|q_h\|^2_{L^2(\Omega)}\|\mathbf{v}_h\|_{H^1(\Omega)}} \geq c_{is} > 0 \tag{4}$$

where c_{is} is the inf-sup constant independent of h.

The discrete velocity approximation $\mathbf{u}_h$ of problem (1) is *in general* not exactly divergence-free, i.e., $\text{div}(\mathbf{u}_h) \neq 0$. A sufficient conditions that guarantees divergence-free velocities is

$$\{\text{div } \mathbf{v} : \mathbf{v} \in V_h\} \subseteq Q_h, \tag{5}$$

which will conflict with (4), unless the equality holds in (5).

The discretization techniques that produce an exactly divergence-free velocity fields are of great practical interest and are not easy to devise in the framework of classical finite elements. In the context of Isogeometric Analysis, a few choices of spline based discrete pairs of spaces (V_h, Q_h) which satisfy (4) have been presented in Buffa et al. [12]. These choices are seen as spline generalization of well known FE spaces, namely Taylor-Hood (TH) elements, Nédélec (N) elements of the second family and Raviart-Thomas (RT) elements. Moreover, the spline generalization of Raviart-Thomas elements introduced in [10] also enjoys property (5) and thus provides divergence-free discrete solutions.

On a rectangular domain Ω with the associated mesh $\mathcal{M}$ the choice of spline spaces (V_h, Q_h) for the Raviart-Thomas (RT) elements can be defined as

$$V_h^{RT} = \mathbb{S}^{p+1,q}_{k+1,\ell}(\mathcal{M}) \times \mathbb{S}^{p,q+1}_{k,\ell+1}(\mathcal{M}); \quad Q_h^{RT} = \mathbb{S}^{p,q}_{k,\ell}(\mathcal{M}); \tag{6}$$

where $\mathbb{S}^{p,q}_{k,\ell}(\mathcal{M})$ denotes the two dimensional spline space of bi-degree (p,q) and continuity (k,ℓ) in the two directions.

In the results of Theorem 3.1 of Buffa et al. [12], a characterization for the range of the div operator in the situations of interest for the Raviart-Thomas elements $V_h \times Q_h$ which ensure the stability and divergence free conforming solutions were presented. In this paper, we extend their characterization (results of Theorem 3.1) for the case of splines spaces over general meshes $\mathcal{M}$. The main result is given as follows:

Theorem 1. *Let $\mathbb{S}^{p+1,q+1}(\mathcal{M})$ be a spline space of bi-degree (p,q) over a general homology*[1] *free box mesh $\mathcal{M}$ on the rectangular domain Ω, then the following pairs of spaces are equal*

$$\{div(\boldsymbol{v}) : \boldsymbol{v} \in V_h\} = \{q \in Q_h\}; \tag{7}$$

$$\{div(\boldsymbol{v}) : \boldsymbol{v} \in V_h,\ \boldsymbol{v}\cdot\boldsymbol{n}|_{\partial\Omega} = 0\} = \{q \in Q_h : \int q = 0\}; \tag{8}$$

$$\{div(\boldsymbol{v}) : \boldsymbol{v} \in V_h,\ \boldsymbol{v}|_{\partial\Omega} = \boldsymbol{0}\} = \{q \in Q_h : \int q = 0 \ \textit{with}, \ q(\boldsymbol{x}_i) = 0, i = 1...4\}; \tag{9}$$

with

$$V_h = \mathbb{S}^{p+1,q}(\mathcal{M}) \times \mathbb{S}^{p,q+1}(\mathcal{M}) \ \textit{and} \ Q_h = \mathbb{S}^{p,q}(\mathcal{M});$$

where $\boldsymbol{n}$ denotes the outward unit normal to the boundary of Ω and $\boldsymbol{x}_i, i = 1, ..., 4$ denote its four corner points.

Proof. The proof of this theorem is given in three steps, as the result of Theorems 2-4 for the case of (7)–(9), respectively, see Section 4. □

Although the results of Theorem 1 have a general significance for spline spaces over a box meshes, we will here consider the structured LR B-spline spaces as introduced by Johannessen et al. [25], which is a subset of LR B-splines, as a suitable candidate for div-compatible splines spaces with local refinement capability.

[1] See discussion in Section 3

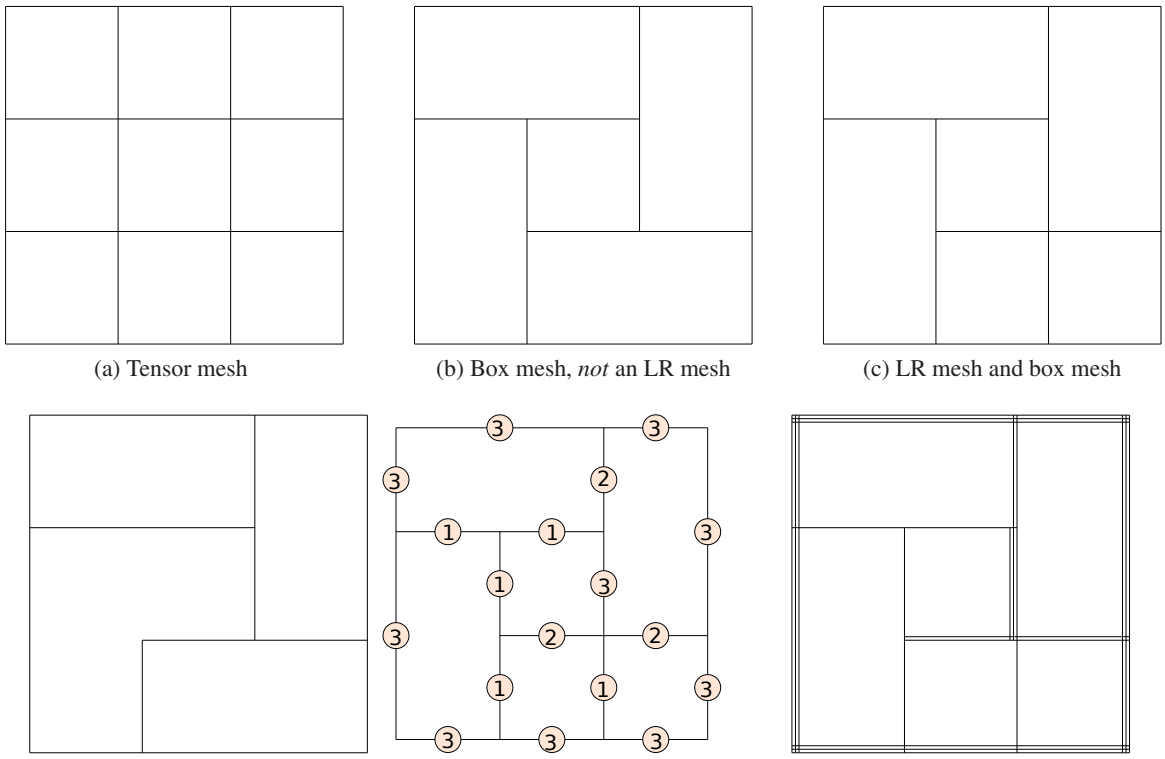

(a) Tensor mesh (b) Box mesh, *not* an LR mesh (c) LR mesh and box mesh

(d) Not an LR-mesh, nor a box mesh (e) LR mesh with multiplicities (f) Alternative way of drawing (e)

Figure 1: Note that there is no way to create the box mesh (b) from single line insertions (starting at tensor mesh) where every intermediate state is also a box mesh. This is a prerequisite for all LR meshes.

3 Spline spaces over planar box meshes

The aim of this section is to set the notations and briefly state the definitions of several types of unstructured meshes and present the dimension of spline spaces over them. The dimension argument was first presented by Mourrain [29] and later extended to multivariate case by Pettersen [31].

In the literature, one can classify several types of unstructured meshes as defined below.

Definition 1. A **Box Mesh** or T-mesh is a partitioning of a two-dimensional rectangular domain $[x_0, x_n] \times [y_0, y_n]$ into smaller rectangles by horizontal and vertical lines.

Definition 2. A **Tensor Mesh** is a box mesh where there are no T-joints, i.e., all horizontal and vertical lines span the entire length $[x_0, x_n]$ or $[y_0, y_n]$.

Definition 3. An **LR-Mesh** $\mathcal{M}_n$ is a box mesh which is the result from a series of single line insertions $\{E_i\}_{i=1}^n$ starting from a tensor mesh $\mathcal{M}_0$, i.e. $\mathcal{M}_n \supset \mathcal{M}_{n-1} \supset ... \supset \mathcal{M}_1 \supset \mathcal{M}_0$ and each intermediate state $\mathcal{M}_{i+1} = \{\mathcal{M}_i \cup E_i\}$ is a also a box mesh.

In other words, it should be possible to create an LR-Mesh by inserting one line at a time, where the lines never stops in the center of an element (knot span) during its creation. Figure 1 shows different types of unstructured meshes.

Definition 4. A box mesh, Tensor Mesh or LR-Mesh **with multiplicities** is a mesh $\mathcal{M}$ where each line segment has a corresponding integer value μ, called the line multiplicity. Each multiplicity must satisfy $0 < \mu \leq s$, where s is the polynomial degree (in x-direction for vertical lines and in y-direction for horizontal lines).

Now we define the spline space $\mathbb{S}^{p,q}(\mathcal{M})$ in term of piecewise polynomials of a given box mesh $\mathcal{M}$ with multiplicities:

$$\mathbb{S}^{p,q}(\mathcal{M}) = \left\{ \varphi|_F \in \mathbb{P}^{p,q} \wedge \varphi|_{E^\perp} \in C^{k(E)} \right\} \tag{10}$$

where $\mathbb{P}^{p,q}$ is polynomials of bi-degree (p, q) and $\mathcal{M} = \{\boldsymbol{F}, \boldsymbol{E}_y, \boldsymbol{E}_x, \boldsymbol{V}\}$ is the mesh defined by the collection of faces F, horizontal edges E_y, vertical edges E_x and vertices V. A continuity k is assigned to each edge and is given by the multiplicity $\mu(E)$ as

$$k(E) = \begin{cases} p - \mu(E), & \text{for vertical edges } E_x \\ q - \mu(E), & \text{for horizontal edges } E_y. \end{cases} \tag{11}$$

Note that vertical lines reduce continuity in the x-direction, and horizontal lines in the y-direction. The notation $\varphi|_{E^\perp}$ in (10) implies evaluation of φ *across* the edge E. We also define an associated horizontal and vertical continuity with each vertex

$$\boldsymbol{k}(V) = \begin{bmatrix} k_1(V) \\ k_2(V) \end{bmatrix} = \begin{bmatrix} \min\{k(E_x)\} \\ \min\{k(E_y)\} \end{bmatrix} \tag{12}$$

where E_x is all vertical edges connected to this particular vertex, and likewise for horizontal edges.

In the case of uniform mesh continuities (k, ℓ), we write $\mathbb{S}^{p,q}_{k,\ell}(\mathcal{M})$. Even if the continuities are implicitly defined in the mesh $\mathcal{M}$ and hence it is possible to drop the continuity subscripts, we feel that they emphasize some key facts and it is illustrative to keep them whenever possible. We also note that all results presented in this paper will hold true for mixed continuities $\mathbb{S}^{p,q}(\mathcal{M})$.

Now using the result from Mourrain [29], it can be shown that the dimension of the spline space $\mathbb{S}^{p,q}(\mathcal{M})$ will be

$$\begin{aligned} \dim\left(\mathbb{S}^{p,q}(\mathcal{M})\right) &= \sum_{F \in \boldsymbol{F}} (p+1)(q+1) \\ &- \sum_{E_x \in \boldsymbol{E}_x} (p+1)(k(E_x)+1) \\ &- \sum_{E_y \in \boldsymbol{E}_y} (q+1)(k(E_y)+1) \\ &+ \sum_{V \in \boldsymbol{V}} (k_1(V)+1)(k_2(V)+1) \\ &+ \mathcal{H}^{p,q}(\mathcal{M}) \end{aligned} \tag{13}$$

where $\mathcal{H}^{p,q}(\mathcal{M})$ denotes the homology term that depends on a given mesh $\mathcal{M}$ and polynomial bi-degree (p, q). The homology is rather cumbersome to handle, but we will see later that all practical meshes considered in this paper have zero homology term. For uniform continuity (k, ℓ) across the entire mesh, and with $\mathcal{H}^{p,q}(\mathcal{M}) = 0$, equation (13) simplifies to

$$\begin{aligned} \dim\left(\mathbb{S}^{p,q}_{k,\ell}(\mathcal{M})\right) &= (p+1)(q+1)\#\mathbf{F} \\ &- (p+1)(\ell+1)\#\mathbf{E}_x \\ &- (q+1)(k+1)\#\mathbf{E}_y \\ &+ (k+1)(\ell+1)\#\mathbf{V} \end{aligned} \tag{14}$$

where $\#\mathbf{F}$ is the number of faces in the mesh, $\#\mathbf{E}_x$ and $\#\mathbf{E}_y$ is the number of interior vertical and horizontal edges, respectively, and $\#\mathbf{V}$ is the number of interior vertices. In the later sections of the paper we shorten the notation and simply write F for the number of faces $\#\mathbf{F}$ and likewise for edges and vertices.

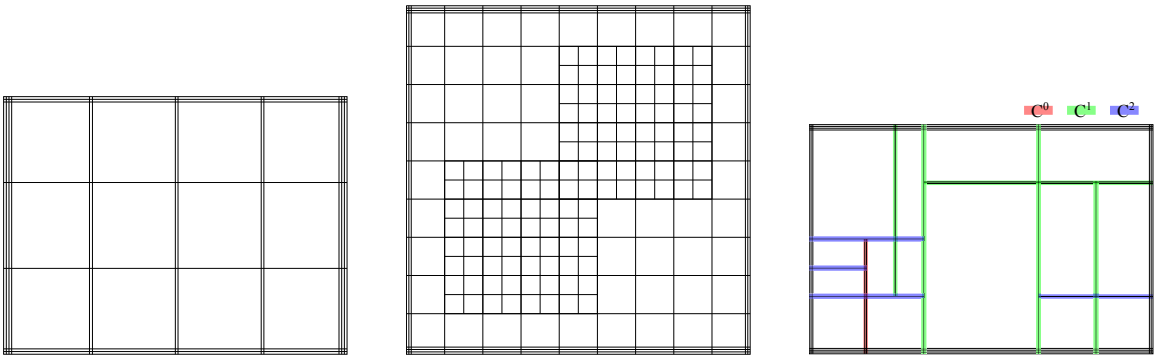

(a) Mesh description:
$p = 3,\ q = 2$
$k = 1,\ \ell = 1$
$\#\mathbf{F} = 12,\ \#\mathbf{V} = 6$
$\#\mathbf{E}_y = 8,\ \#\mathbf{E}_x = 12$
$\dim(\mathbb{S}^{p,q}_{k,\ell}) = 50$ according to (14)

(b) Mesh description:
$p = 2,\ q = 3$
$k = 1,\ \ell = 2$
$\#\mathbf{F} = 174,\ \#\mathbf{V} = 171$
$\#\mathbf{E}_y = 172,\ \#\mathbf{E}_x = 172$
$\dim(\mathbb{S}^{p,q}_{k,\ell}) = 190$ according to (14)

(c) Mesh description:
$p = 2,\ q = 3,$
mixed continuity
$\#\mathbf{F} = 15,\ \#\mathbf{V} = 12$
$\#\mathbf{E}_y = 12,\ \#\mathbf{E}_x = 14$
$\dim(\mathbb{S}^{p,q}) = 38$ according to (13)

Figure 2: The dimension of different spline spaces $\mathbb{S}^{p,q}$ over box-meshes $\mathcal{M}$ of bi-degree (p, q) and varying smoothness (k, ℓ).

Proposition 1. *For an LR mesh $\mathcal{M}$, a sufficient condition for the homology term $\mathcal{H}^{p,q}(\mathcal{M})$ to be zero is that it is constructed of horizontal lines spanning $p + 1$ elements and vertical lines spanning $q + 1$ elements.*

Proof. For this consult Pettersen [31]. □

3.1 Derivative spaces

The derivative spaces of $\mathbb{S}^{p,q}(\mathcal{M})$ defined as a piecewise polynomial space in (10) over an arbitrary box mesh $\mathcal{M}$ can be defined as follows:

Definition 5. Let $\{\varphi_i\}_{i=1}^n$ be a basis for the space $\mathbb{S}^{p,q}(\mathcal{M})$ as defined in (10). Then both components of the **derivative spaces** can be defined as

$$\partial_x \mathbb{S}^{p,q}(\mathcal{M}) = \text{span}\left\{\frac{\partial}{\partial x}\varphi_i(x,y)\right\}_{i=1}^n \tag{15}$$

$$\partial_y \mathbb{S}^{p,q}(\mathcal{M}) = \text{span}\left\{\frac{\partial}{\partial y}\varphi_i(x,y)\right\}_{i=1}^n. \tag{16}$$

We make the following observation about the derivative spaces of Definition 5.

Proposition 2. *Let $\mathcal{M}$ be an arbitrary box mesh with multiplicities and $\mathbb{S}^{p,q}(\mathcal{M})$ be a spline space over $\mathcal{M}$. Then we obtain*

$$\partial_x \mathbb{S}^{p,q}(\mathcal{M}) \subseteq \mathbb{S}^{p-1,q}(\mathcal{M}) \tag{17}$$

$$\partial_y \mathbb{S}^{p,q}(\mathcal{M}) \subseteq \mathbb{S}^{p,q-1}(\mathcal{M}). \tag{18}$$

Proof. For a given $\varphi \in \mathbb{S}^{p,q}(\mathcal{M})$, under the x-derivative operation, the polynomial degree is reduced by one, i.e. $\frac{\partial \varphi}{\partial x}|_F \in \mathbb{P}^{p-1,q}$, and the continuity across vertical directions are also reduce by one, i.e. $\frac{\partial \varphi}{\partial x}|_{E_x} \in C^{k(E_x)}$, where $k(E_x) = p - 1 - \mu(E_x)$ with the edge multiplicity $\mu(E_x)$. While the continuity across horizontal edges remains unchanged. Hence $\frac{\partial \varphi}{\partial x} \in \mathbb{S}^{p-1,q}(\mathcal{M})$. The proof of (18) is analogous. □

Proposition 3. *Let $\mathcal{M}$ be a tensor mesh with uniform multiplicities, i.e. $\mu(E_x) = p - k,\ \forall E_x$ and $\mu(E_y) = q - \ell,\ \forall E_y$ with (k, ℓ) being global continuities in each direction. Then*

$$\partial_x \mathbb{S}^{p,q}_{k,\ell}(\mathcal{M}) = \mathbb{S}^{p-1,q}_{k-1,\ell}(\mathcal{M}) \tag{19}$$

Proof. See [10] for the proof. □

The results of Proposition 3 does not hold for general box meshes. For a counter example see Figure 3, where we show a box mesh on which the derivative space is *not* the space of all polynomials of one less degree and continuity.

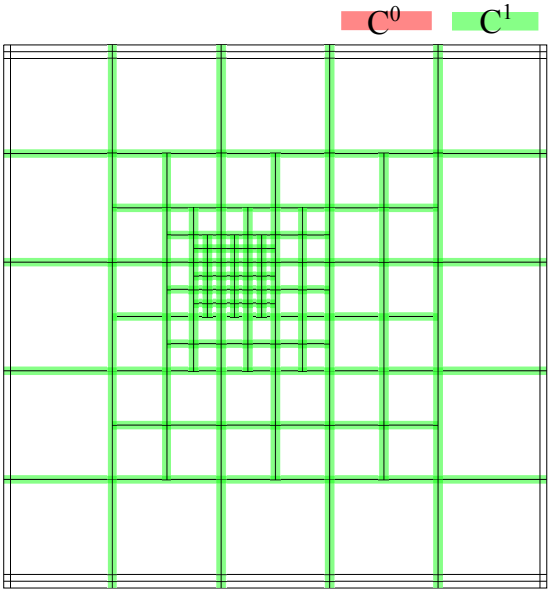

(a) Mesh description of $\mathbb{S}^{p,q}_{k,\ell}(\mathcal{M})$ with
$p = 2,\ q = 2,\ k = 1,\ \ell = 1$
$\#F = 106,\ \#V = 115$
$\#E_H = 110,\ \#E_V = 110$
$\dim(\mathbb{S}^{p,q}_{k,\ell}) = 94$ according to (14)

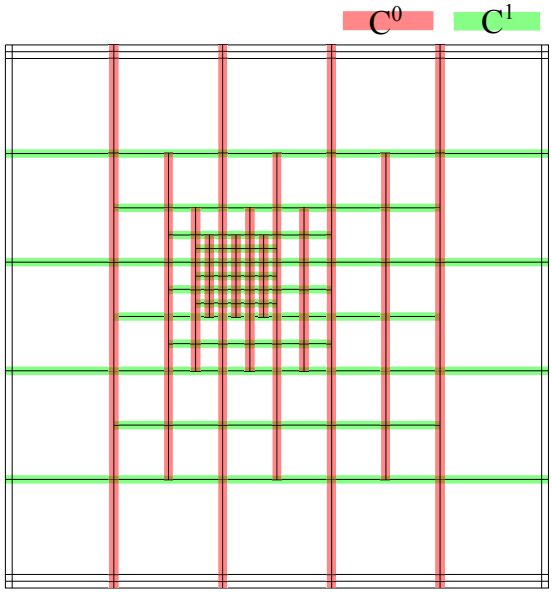

(b) Mesh description of $\mathbb{S}^{p,q}_{k,\ell}(\mathcal{M})$ with
$p = 1,\ q = 2,\ k = 0,\ \ell = 1$
$\#F = 106,\ \#V = 115$
$\#E_H = 110,\ \#E_V = 110$
$\dim(\mathbb{S}^{p,q}_{k,\ell}) = 96$ according to (14)

Figure 3: **Derivative spaces:** *A counter example*: On this box mesh, It is shown that the derivative space is *not* the space of all polynomials of one less degree and continuity: $\partial_x \mathbb{S}^{p,q}_{k,\ell}(\mathcal{M}) \neq \mathbb{S}^{p-1,q}_{k-1,\ell}(\mathcal{M})$ since $\dim(\mathbb{S}^{p-1,q}_{k-1,\ell}(\mathcal{M})) > \dim(\mathbb{S}^{p,q}_{k,\ell}(\mathcal{M}))$. The continuity colours are derived from the edge multiplicities which are the same for both figures.

4 The spline complex over box meshes

We note that the results of this section will hold true for any properly defined spline spaces over box meshes. We consider the dimensionality argument approach to prove the compatibility in the spline spaces, where the dimensional formula's of Mourrain [29] for box meshes is used as a main tool. Thus it becomes a requirement that the spline spaces should span the full space of piecewise smooth polynomials given by (13).

Theorem 2. *Let $\mathcal{M}$ be a given box mesh with multiplicities and $\mathbb{S}^{p+1,q+1}(\mathcal{M})$ be a spline space as defined in* (10)*. If the homology term $\mathcal{H}^{p+1,q+1}(\mathcal{M}) = 0$, then the spline spaces X_h^0, X_h^1 and X_h^2 form a De Rham complex and the following sequence is exact*

$$\mathbb{R} \to X_h^0 \xrightarrow{\textit{rot}} X_h^1 \xrightarrow{\textit{div}} X_h^2 \to 0 \tag{20}$$

where

$$\begin{aligned} X_h^0 &= \mathbb{S}^{p+1,q+1}(\mathcal{M}) \\ X_h^1 &= \mathbb{S}^{p+1,q}(\mathcal{M}) \times \mathbb{S}^{p,q+1}(\mathcal{M}) \\ X_h^2 &= \mathbb{S}^{p,q}(\mathcal{M}). \end{aligned}$$

Proof. The proof follows the same structure as outlined by Buffa el al. [13]. To prove (20), we need to show the following:

$$\mathbb{R} = \ker(\mathbf{rot}) \tag{21}$$

$$\mathrm{im}(\mathbf{rot}) = \ker(\mathrm{div}) \tag{22}$$

$$\mathrm{im}(\mathrm{div}) = X_h^2, \tag{23}$$

where $\mathbf{rot}(\varphi) = [\partial_y\varphi, -\partial_x\varphi]^T$ and $\mathrm{div}(\boldsymbol{u}) = \partial_x u_1 + \partial_y u_2$.

The proof of (21) is straightforward. We observe that

$$\varphi \in X_h^0 : \mathbf{rot}(\varphi) = [0,0]^T \Leftrightarrow \varphi = c \in \mathbb{R}.$$

Hence $\mathbb{R} = \ker(\mathbf{rot})$.

To prove (22), we first note that

$$\mathrm{im}(\mathbf{rot}) \subseteq \ker(\mathrm{div}) \;\text{ since }\; \forall\varphi \in X_h^0 \Rightarrow \mathrm{div}(\mathbf{rot}(\varphi)) = 0.$$

Conversely to show $\mathrm{im}(\mathbf{rot}) \supseteq \ker(\mathrm{div})$, assume $\mathrm{div}(\boldsymbol{u}) = 0$. Then there exists an $\varphi \in X_h^0$ such that $\boldsymbol{u} = \mathbf{rot}(\varphi)$ and φ is given as

$$\varphi(x,y) = -\int_0^x u_2(t,0)\,dt + \int_0^y u_1(x,t)\,dt.$$

The proof of (23) is based on a dimensionality argument of the spline spaces. First using Proposition 2 we obtain $\mathrm{im}(\mathrm{div}) \subseteq X_h^2$. Now to establish equality we need to show that the dimensions of both spaces are equal, i.e.,

$$\begin{aligned} \dim(\mathrm{im}(\mathrm{div})) &= \dim(X_h^1) - \dim(\ker(\mathrm{div})) \\ &= \dim(X_h^1) - \dim(\mathrm{im}(\mathbf{rot})) \\ &= \dim(X_h^1) - \dim(X_h^0) + \dim(\ker(\mathbf{rot})) \\ &= \dim(X_h^1) - \dim(X_h^0) + 1. \end{aligned} \tag{24}$$

After assuming the uniform continuity over the mesh $\mathcal{M}$ we obtain from (14):

$$\begin{aligned}
\dim(\mathbb{S}^{p+1,q+1}_{k+1,l+1}) &= (p+2)(q+2)F - (p+2)(l+2)E_y - (q+2)(k+2)E_x + (k+2)(l+2)V \\
\dim(\mathbb{S}^{p+1,q}_{k+1,l}) &= (p+2)(q+1)F - (p+2)(l+1)E_y - (q+1)(k+2)E_x + (k+2)(l+1)V \\
\dim(\mathbb{S}^{p,q+1}_{k,l+1}) &= (p+1)(q+2)F - (p+1)(l+2)E_y - (q+2)(k+1)E_x + (k+1)(l+2)V \\
\dim(\mathbb{S}^{p,q}_{k,l}) &= (p+1)(q+1)F - (p+1)(l+1)E_y - (q+1)(k+1)E_x + (k+1)(l+1)V.
\end{aligned}$$

Using (24), the problem reduce to

$$\begin{aligned}
\dim(X^2_h) &= \dim(X^1_h) - \dim(X^0_h) + 1 \\
\dim(\mathbb{S}^{p,q}_{k,l}) &= \dim(\mathbb{S}^{p+1,q}_{k+1,l}) + \dim(\mathbb{S}^{p,q+1}_{k,l+1}) - \dim(\mathbb{S}^{p+1,q+1}_{k+1,l+1}) + 1
\end{aligned}$$

which can be done once we realize that the Euler characteristic of a planar graph is 1, i.e.

$$F - E_x - E_y + V = 1.$$

Note that the assumption on the uniform continuity used here is not required as it is possible to obtain the same conclusion by using (13) in (24). □

The main aim of the paper is to show the use of locally refined div-compatible spline spaces in mixed FE discretizations to solve incompressible flow problems. Thus we now present the extension of a De Rhams complex result of Theorem 2 after imposing the boundary conditions on the velocity field. We consider two main cases of imposing the boundary conditions.

4.1 No penetration boundary conditions

The No penetration boundary condition on the velocity is defined by $\boldsymbol{u} \cdot \boldsymbol{n} = 0$ on the domain boundary. In order to produce an exact De Rham complex, we need to impose corresponding boundary conditions for the other spaces.

Theorem 3. *Let $\mathcal{M}$ be a given box mesh with multiplicities and $\mathbb{S}^{p+1,q+1}(\mathcal{M})$ be a spline space as defined in* (10)*. If the homology term $\mathcal{H}^{p+1,q+1}(\mathcal{M}) = 0$, then the spline spaces Y^0_h, Y^1_h and Y^2_h form a De Rham complex and the following sequence is exact*

$$0 \to Y^0_h \xrightarrow{\textbf{\textit{rot}}} Y^1_h \xrightarrow{div} Y^2_h \xrightarrow{\int} 0 \tag{25}$$

where

$$\begin{aligned}
Y^0_h &= \{\varphi \in \mathbb{S}^{p+1,q+1}(\mathcal{M}) &&: \ \varphi = 0 \text{ on } \Gamma\} \\
Y^1_h &= \{\boldsymbol{u} \in \mathbb{S}^{p+1,q}(\mathcal{M}) \times \mathbb{S}^{p,q+1}(\mathcal{M}) &&: \ \boldsymbol{u} \cdot \boldsymbol{n} = 0 \text{ on } \Gamma\} \\
Y^2_h &= \{p \in \mathbb{S}^{p,q}(\mathcal{M}) &&: \ \textstyle\int_\Omega p = 0\}.
\end{aligned}$$

Here Γ is the boundary of our domain and $\boldsymbol{n}$ is the outward pointing unit normal.

Proof. The proof follows the main structure of Theorem 2. The main difference in the proof is to show that $\mathrm{im}(\mathrm{div}) = Y^2_h$. For this, we need to introduce the exterior edges and vertices along the boundary of our domain to account for the lost degrees of freedom when imposing the constraints. Let E^E_y, E^E_x, V^E_y and V^E_x denote the number of horizontal edges (at the top/bottom of our domain), vertical edges (left-/right), horizontal vertices (top/bottom) and vertical vertices (left/right), respectively. Here, we do not count the four corner vertices among V^E_x and V^E_y as these do not contribute to inter-element regularity. Then we obtain

$$\begin{aligned}
\dim(Y^0_h) &= \dim(\mathbb{S}^{p+1,q+1}_{k+1,l+1}) - (p+2)E^E_y - (q+2)E^E_x + (k+2)V^E_y + (l+2)V^E_x + 4 \\
\dim(Y^{1,1}_h) &= \dim(\mathbb{S}^{p+1,q}_{k+1,l}) - (q+1)E^E_x + (l+1)V^E_x \\
\dim(Y^{1,2}_h) &= \dim(\mathbb{S}^{p,q+1}_{k,l+1}) - (p+1)E^E_y + (k+1)V^E_y \\
\dim(Y^2_h) &= \dim(\mathbb{S}^{p,q}_{k,l}) - 1.
\end{aligned}$$

□

The term $+4$ in the first line is due to the four corners being constrained twice in the four terms prior to this. Realizing that $\dim(\ker(\mathbf{rot})) = 0$, due to the boundary conditions, we have to show the dimension equality

$$\dim(Y_h^2) = \dim(Y_h^1) - \dim(Y_h^0).$$

Here we use the fact that splitting a boundary curve into edges and vertices, we have the formula: $E_y^E - V_y^E = 1$, which is enough to prove that the dimensions match.

4.2 No slip boundary conditions

The No slip boundary condition on the velocity field is defined by $\boldsymbol{u} = \mathbf{0}$ on the boundary. Again, we will need to provide corresponding restraints on the accompanying spaces (pressure and potential) to make the spline complex exact.

Theorem 4. *Let $\mathcal{M}$ be a given box mesh with multiplicities and $\mathbb{S}^{p+1,q+1}(\mathcal{M})$ be a spline space as defined in* (10)*. If the homology term $\mathcal{H}^{p+1,q+1}(\mathcal{M}) = 0$, then the spline spaces Z_h^0, Z_h^1 and Z_h^2 form a De Rham complex and the following sequence is exact*

$$0 \to Z_h^0 \xrightarrow{\textit{rot}} Z_h^1 \xrightarrow{\textit{div}} Z_h^2 \xrightarrow{\int} 0 \tag{26}$$

where

$$\begin{array}{rcll} Z_h^0 & = & \{\varphi \in \mathbb{S}^{p+1,q+1}(\mathcal{M}) & : \ \varphi = 0 \ \wedge \ \frac{\partial \varphi}{\partial \boldsymbol{n}} = 0 \textit{ on } \Gamma\} \\ Z_h^1 & = & \{\boldsymbol{u} \in \mathbb{S}^{p+1,q}(\mathcal{M}) \times \mathbb{S}^{p,q+1}(\mathcal{M}) & : \ \boldsymbol{u} = \mathbf{0} \textit{ on } \Gamma\} \\ Z_h^2 & = & \{p \in \mathbb{S}^{p,q}(\mathcal{M}) & : \ \int_\Omega p = 0 \ \wedge \ p(x_i) = 0 \ , \ i = \{1...4\}\} \end{array}$$

and $\mathcal{M}$ is a box mesh with multiplicities. Here Γ is the boundary of our domain and $\boldsymbol{n}$ is the outward pointing unit normal while x_i are the four corner points.

Proof. The proof here follows a similar structure of the dimensionality argument as above and we obtain

$$\begin{array}{rcl} \dim(Z_h^0) & = & \dim(\mathbb{S}_{k+1,l+1}^{p+1,q+1}) - 2(p+2)E_y^E - 2(q+2)E_x^E + 2(k+2)V_y^E + 2(l+2)V_x^E + 16 \\ \dim(Z_h^{1,1}) & = & \dim(\mathbb{S}_{k+1,l}^{p+1,q}) - (p+2)E_y^E - qE_x^E + (k+2)V_y^E + lV_x^E + 4 \\ \dim(Z_h^{1,2}) & = & \dim(\mathbb{S}_{k,l+1}^{p,q+1}) - (p+1)E_y^E - (q+2)E_x^E + (k+1)V_y^E + (l+2)V_x^E + 4 \\ \dim(Z_h^2) & = & \dim(\mathbb{S}_{k,l}^{p,q}) - 5 \end{array}$$

To impose both the function value, and its normal derivative, we count the 4 corners and their associated normals twice and hence we need to add 16 to compensate. Again, we have that $\dim(\ker(\mathbf{rot})) = 0$, and the dimension equality

$$\dim(Z_h^2) = \dim(Z_h^1) - \dim(Z_h^0),$$

which can be verify by standard arithmetics. □

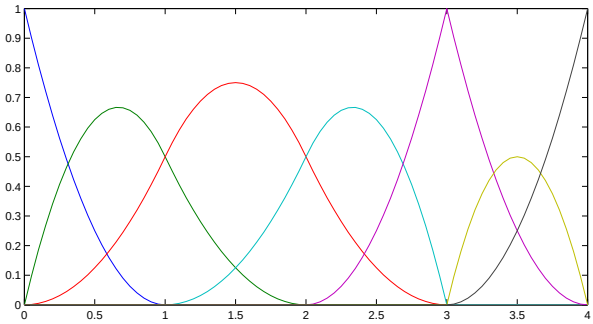

Figure 4: All quadratic basis functions generated by the knot $\Xi = [0, 0, 0, 1, 2, 3, 3, 4, 4, 4]$. Each individual basis function can be described using a local knot vector of length 4.

5 LR-splines

In this section we will show how to construct a spline basis. We first introduce the traditional tensor product B-splines as defined by the Cox-de Boor recursion formula, and then continue by presenting locally refined (LR) B-splines. While these allow for quite general meshes, our focus will be the subclass arising from the refinement scheme and our adaptive solvers. These are denoted "structured mesh refinement" and are discussed in the last part of this section.

5.1 Univariate B-splines

Consider a knot vector of non-decreasing knots $\{x_i\}_{i=1}^{n+p+1}$. By elementary spline theory, we can construct a basis on the domain $[x_{p+1}, x_{n+1}]$ by piecewise smooth polynomials using the Cox-de Boor recursion formula

$$\begin{aligned} N_{i,p}(x) &= \frac{x - x_i}{x_{i+p} - x_i} N_{i,p-1}(x) + \frac{x_{i+p+1} - x}{x_{i+p+1} - x_{i+1}} N_{i-1,p-1}(x) \\ N_{i,0}(x) &= \begin{cases} 1 & \text{if } x_i \leq x < x_{i+1} \\ 0 & \text{else} \end{cases} \end{aligned} \tag{27}$$

where, by slight abuse of notation, we define that $\frac{0}{0} := 0$. It is customary (but not required) that the knot vector is *open*, that is, the first $p+1$ entries as well as the last $p+1$ entries are equal. In Figure 4 we show an example of a basis constructed on a uniform open knot vector. We will in the following refer to the basis functions $N_{i,p}(x)$ as B-splines. The knot vector holds all the information of the basis constructed. In particular, the following is true

- the B-splines N_i are polynomial and C^∞ in between the knots
- the B-splines are C^{p-m} at the knots, where m is the knot multiplicity
- each B-spline is dependent on exactly $p + 2$ knots.

It is the last point, which will allow us to define a local knot vector corresponding to each B-spline, and this observation will be utilized below to introduce LR B-splines.

Definition 6. A **local knot vector** of degree p is a knot vector $\Xi \in \mathbb{R}^{p+2}$ consisting of exactly $p + 2$ non-decreasing knots $\{x_i\}_{i=1}^{p+2}$.

One interpretation of local knot vectors is that they are ordinary knot vectors corresponding to a single basis function, i.e. $n = 1$.

Definition 7. A bivariate **B-spline** $B(x, y)$ of bi-degree (p, q) is a separable function $B : \mathbb{R}^2 \to \mathbb{R}$

$$B_{\Xi,\Psi}(x, y) = N_\Xi(x)N_\Psi(y) \tag{28}$$

defined by the local knot vectors $\Xi \in \mathbb{R}^{p+2}$ and $\Psi \in \mathbb{R}^{q+2}$, where $N_\Xi(x)$ and $N_\Psi(y)$ are univariate B-spline functions defined by the Cox-de Boor recursion formula (27).

We will often just denote a single B-spline by B_i where it is understood that the local knot vectors Ξ and Ψ are constructed using the refinement algorithm below.

5.2 Refinement of B-splines

At the core of the local refinement, i.e. knot insertion, rests the fact that a single coarse B-spline may be described using a linear combination of two finer B-splines, their relation given by

$$N_\Xi(x) = \alpha_1 N_{\Xi_1}(x) + \alpha_2 N_{\Xi_2}(x), \tag{29}$$

where

$$\begin{aligned} \alpha_1 &= \begin{cases} 1, & x_{p+1} \le \hat{x} \le x_{p+2} \\ \frac{\hat{x}-x_1}{x_{p+1}-x_1}, & x_1 \le \hat{x} \le x_{p+1} \end{cases} \\ \alpha_2 &= \begin{cases} \frac{x_{p+2}-\hat{x}}{x_{p+2}-x_2}, & x_2 \le \hat{x} \le x_{p+2} \\ 1, & x_1 \le \hat{x} \le x_2 \end{cases} \end{aligned} \tag{30}$$

and the knot vectors are

$$\begin{aligned} \Xi &= [x_1, x_2, ...x_{i-1}, \quad x_i, ...x_{p+1}, x_{p+2}] \\ \Xi_1 &= [x_1, x_2, ...x_{i-1}, \hat{\boldsymbol{x}}, \ x_i, ...x_{p+1} \quad\ ] \\ \Xi_2 &= [\quad x_2, ...x_{i-1}, \hat{\boldsymbol{x}}, \ x_i, ...x_{p+1}, x_{p+2}]. \end{aligned}$$

Note that the insertion of the knot $\hat{x}$ into Ξ yields a knot vector of size $p + 3$, meaning that it is generating two B-splines. These two B-splines are described by the local knot vectors Ξ_1 and Ξ_2, both of size $p + 2$.

Let us look at an example using this technique. Say we want to insert $\hat{x} = \frac{3}{2}$ into the B-spline $\Xi_3 = [0, 1, 2, 3]$. This would give us $\alpha_1 = \alpha_2 = \frac{3}{4}$ and the three functions are plotted in Figure 5. If one were to insert the knot $\hat{x} = \frac{3}{2}$ into the *set* of B-splines in Figure 4, then this will require two more functions to be split, namely the function $\Xi_2 = [0, 0, 1, 2]$ and $\Xi_4 = [1, 2, 3, 3]$. All the three splitting shown in Figure 5–6 will then take place. This insertion will replace three old B-splines with four new linearly independent B-splines (see the knot vectors in the figure legend to identify the four distinctive new B-splines).

Bivariate functions are refined in one parametric direction at a time. Using the fact that they are separable we are able to reuse (29) to split one direction and reassemble the bivariate functions after. This can be done as follows

$$\begin{aligned} B_{\boldsymbol{\Xi}}(x, y) &= B_\Xi(x)B_\Psi(y) \\ &= (\alpha_1 B_{\Xi_1}(x) + \alpha_2 B_{\Xi_2}(x))\, B_\Psi(y) \\ &= \alpha_1 B_{\boldsymbol{\Xi}_1}(x, y) + \alpha_2 B_{\boldsymbol{\Xi}_2}(x, y). \end{aligned} \tag{31}$$

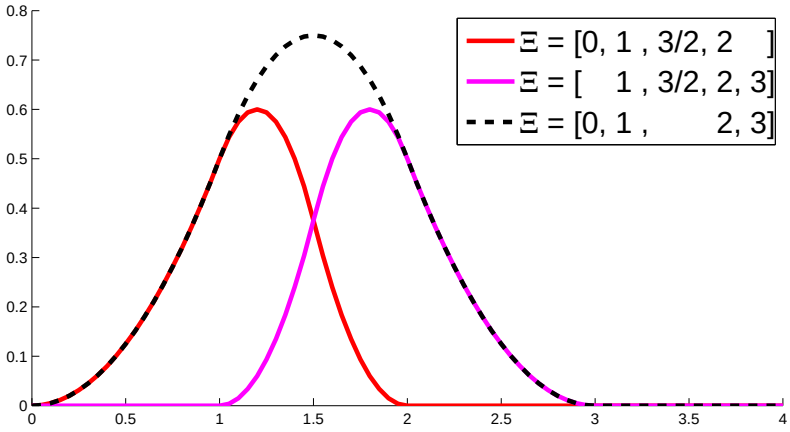

Figure 5: Splitting the B-spline $\Xi = [0, 1, 2, 3]$ into two separate B-splines by inserting the knot $\frac{3}{2}$.

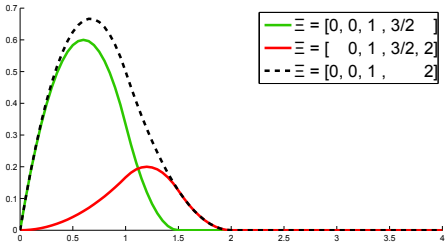

(a) Inserting $x = \frac{3}{2}$ in $\Xi = (0, 0, 1, 2)$.

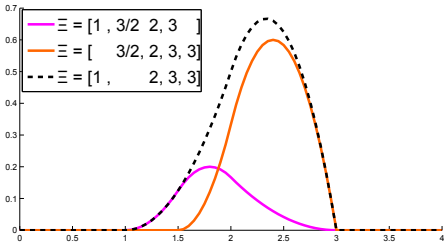

(b) Inserting $x = \frac{3}{2}$ in $\Xi = (1, 2, 3, 3)$.

Figure 6: Displaying function splitting in the case that $\hat{x}$ is not at the knotvector center.

5.3 Local refinement algorithm

When talking about LR B-splines, we usually distinguish between the mesh $\mathcal{M}$ and the set of B-splines $\mathbb{S}$. The mesh is limited to an LR mesh (see Definition 3) and is represented by the set of all lines; vertical and horizontal. The function space $\mathbb{S}$ is represented by the B-splines themselves, which are uniquely determined by their local knot vectors. The refinement algorithm is the interplay in between these two entities and is categorized by two operations: traversing and splitting.

Definition 8. A line in the mesh $\mathcal{M}$ is said to **traverse** a B-spline B_i if it passes through its support, and all of its support.

See Figure 7 for examples on traversing meshlines.

Definition 9. A knot-line is said to **exist** in a B-spline $B_{\Xi,\Psi}$ if its (constant) knot value is represented in Ξ for vertical lines or Ψ for horizontal lines.

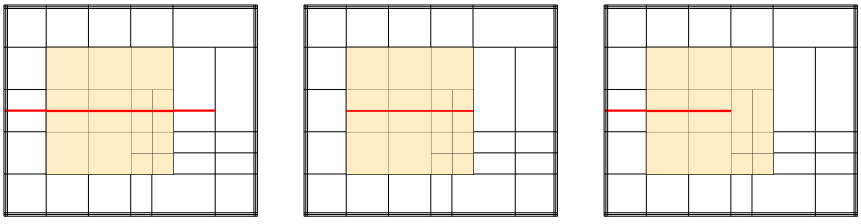

(a) Line traversing B (b) Line traversing B (c) Line not traversing B

Figure 7: Traversing the support of a basis function.

Definition 10. A B-spline B_i can be **split** at the knot x (or y) by the application of (31) producing two new B-splines B_1 and B_2. When inserting the two new B-splines into the existing space $\mathbb{S}$, we either update their control points and weights (if any) if they exist already, or create a new entry if they do not exist.

Note that the B-splines are uniquely determined by their local knot vector, and this is used to identify equal (existing) B-splines. Moreover we note the earlier remark on the weights and the control points. The first is a simple multiplication of the B-spline by some scalar γ to maintain the partition of unity, while the second is the control points, often used for the representation of geometric mappings. The weights are optional, in the sense that they offer nothing in terms of the span of the functions (they do however affect numerical stability). The control points are optional if we are not considering a geometric mapping, but rather is only working in the parametric space.

Algorithm 1 Refinement algorithm

```
1: Insert new line E
2: for every B-spline B_i ∈ 𝕊 do
3:    if E traverse B_i and E does not exist in B_i then
4:       split B_i
5:    end if
6: end for
7: for every newly created B-spline B_j from line 4 or 10 do
8:    for every existing line E ∈ ℳ do
9:       if E traverse B_j and E does not exist in B_j then
10:         split B_j
11:      end if
12:   end for
13: end for
```

We have in this section deliberately simplified several points in the presentation. For a more technical introduction (including details on the weights and control points) we refer the reader to [15] or [25]. For our discussion in this paper however, it is enough to consider the functions as defined in the parametric domain and without weights.

A motivational factor for the use of LR B-splines with spline complexes in Section 4 is their direct construction on the mesh. The integration mesh is the same as the LR mesh where the edge multiplicities are used to construct the reduced continuity lines. For implementation purposes this allows the user to work on a common mesh $\mathcal{M}$, and construct several sets of basis functions $\mathbb{S}^{p+1,q+1}(\mathcal{M})$, $\mathbb{S}^{p+1,q}(\mathcal{M})$, $\mathbb{S}^{p,q+1}(\mathcal{M})$ and $\mathbb{S}^{p,q}(\mathcal{M})$. This not only speeds up computation, but also reduces implementation complexity.

5.4 The LR B-spline complex

We will in this section present the structured mesh refinement as introduced in [25]. It has been shown to provide optimal convergence rates under adaptive refinement for a number of problems containing singularities or rough right-hand sides and we consider it a good choice for our local refinement strategy.

Definition 11. A **B-spline refinement** on an LR spline $\mathcal{L} = \{\mathcal{M}, \mathbb{S}\}$ is a refinement scheme where one B-spline $B \in \mathbb{S}$ dictates a set of meshline insertions such that the largest knotspan of the local knot vector in B is halved.

See Figure 8 for an example B-spline refinement.

Definition 12. A **Structured LR Mesh** of degree (p, q) is a box mesh resulting from a series of B-spline refinements on an LR spline.

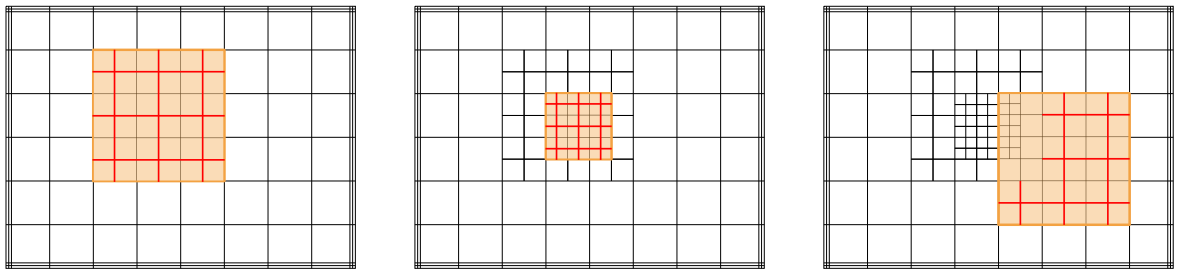

(a) Iteration 1 (b) Iteration 2 (c) Iteration 3

Figure 8: Three iterations of an example B-spline refinement given in definition 11. Notice that we at each iteration halve the largest supported elements. A selection of LR B-splines over the mesh from iteration 3 is depicted in Figure 9

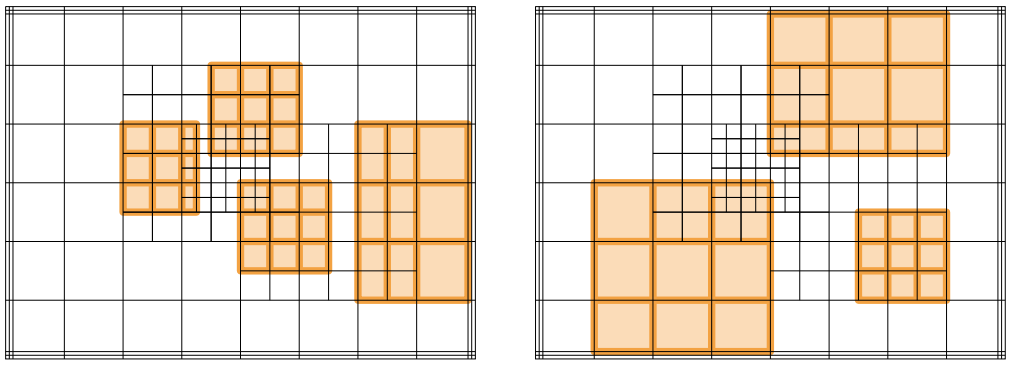

(a) (b)

Figure 9: Some example quadratic LR B-splines over the LR mesh from Figure 8c

We note that the structured LR B-splines and Hierarchical refined B-splines may produce similar meshes. However, as shown in [24] they are in general not identical, and they produce finite element matrices with different sparsity patterns and conditioning numbers.

Proposition 4. *Any structured LR mesh has homology term $\mathcal{H}^{p,q}(\mathcal{M})$ equal to zero.*

Proof. Since every B-spline knot in the local knot vector is appearing in the mesh, and the knot vectors are composed of $p+2$ and $q+2$ knots respectively, we know that each B-spline will span at least $(p+1)\times(q+1)$ elements. Every new line inserted into the mesh will span this length and hence the homology term never increases. Since our initial mesh: a tensorial mesh, has $\mathcal{H}=0$ the proof is complete. □

Proposition 5. *A structured LR mesh of degree (p,q) is also a structured mesh of all degrees $(\hat{p},\hat{q})$, where $\hat{p}\leq p$ and $\hat{q}\leq q$.*

Proof. We here note that the definition of structured LR mesh is linked to the polynomial degree of the basis constructed on it. For tensor products, we have that every lower order function is completely contained in the support of a function of larger polynomial degree; in both directions. Due to Algorithm 1, when a larger B-spline split, we note that the lower order functions will also be split. Any B-spline of bi-degree (p,q) is thus guaranteed to contain enough functions of lower degree to span it's own support. □

The contrary is not the case. For a structured mesh of bi-degree (p,q), it is not guaranteed that it will be for degree $(p+1,q)$ or $(p,q+1)$.

We now are able to construct our spline complex which we will use to discretize the Stokes equations. Consider the four LR splines given on the same structured mesh $\mathcal{M}$ of degree $(p+1,q+1)$

$$
\begin{aligned}
\mathcal{L}^0 &= \{\mathcal{M}, \mathbb{S}^{p+1,q+1}\} \\
\mathcal{L}^{1,1} &= \{\mathcal{M}, \mathbb{S}^{p+1,q}\} \\
\mathcal{L}^{1,2} &= \{\mathcal{M}, \mathbb{S}^{p,q+1}\} \\
\mathcal{L}^2 &= \{\mathcal{M}, \mathbb{S}^{p,q}\}.
\end{aligned}
$$

In order to remain a structured mesh and satisfy a complete De Rham complex, we let the highest degree dictate the B-spline refinements which will drive our adaptive solvers. Let the velocity be given on $\mathcal{L}^{1,1} \times \mathcal{L}^{1,2}$ and the pressure be given on $\mathcal{L}^2$. Setting the LR B-splines $\mathbb{S}$ as the compatible spaces, we have

$$
\begin{aligned}
X_h^0 &= \mathbb{S}^{p+1,q+1} \\
X_h^1 &= \mathbb{S}^{p+1,q} \times \mathbb{S}^{p,q+1} \\
X_h^2 &= \mathbb{S}^{p,q}
\end{aligned}
$$

without boundary conditions. Replace X with Y or Z for no-penetration or no-slip boundary conditions, respectively. In Figure 10 we show an example structured LR mesh with varying continuities. Figure 11 shows the corresponding LR B-splines basis representation constructed on the same mesh. By constructing them with different polynomial degrees, we ensure they form a complete De Rham complex.

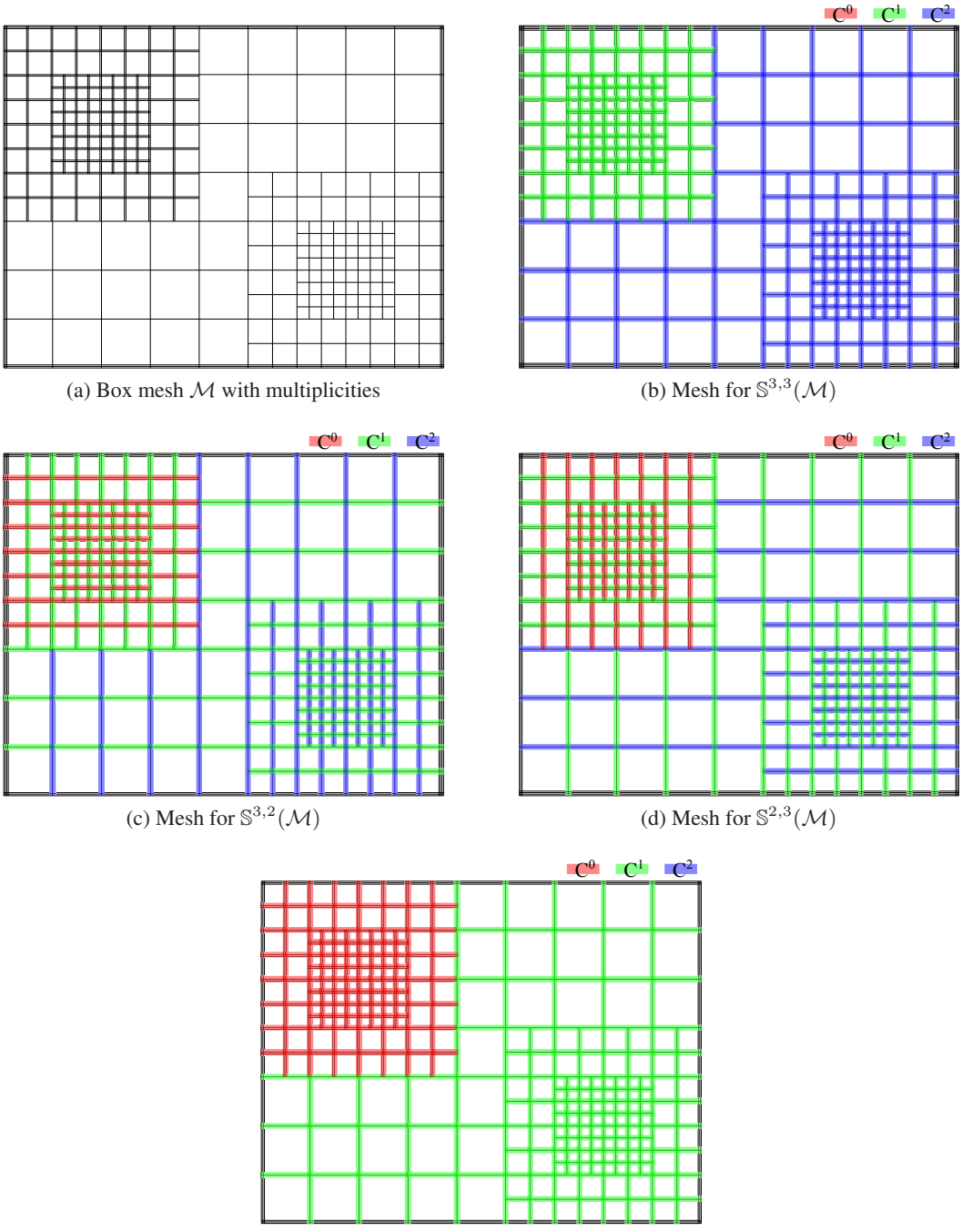

(a) Box mesh $\mathcal{M}$ with multiplicities

(b) Mesh for $\mathbb{S}^{3,3}(\mathcal{M})$

(c) Mesh for $\mathbb{S}^{3,2}(\mathcal{M})$

(d) Mesh for $\mathbb{S}^{2,3}(\mathcal{M})$

(e) Mesh for $\mathbb{S}^{2,2}(\mathcal{M})$

Figure 10: Example spline spaces over a box mesh $\mathcal{M}$ with multiplicities. Note that it is the same mesh which is used for all figures. The continuity is derived from the polynomial degree of the basis as well as the knotline multiplicity. To construct the spline complex we let X_h^0 be given over (b), X_h^1 be given over (c) and (d), while X_h^2 is defined over (e). When solving the Stokes problem, we let the velocity $\boldsymbol{u}_h \in X_h^1$ and the pressure $p_h \in X_h^2$. The basis functions of X_h^0 is used for refinement purposes to ensure that the De Rham diagram is exact and all meshes are legal.

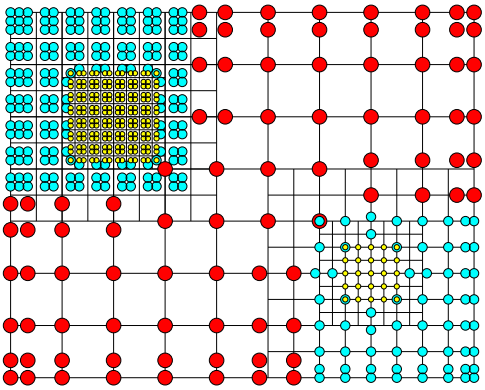

(a) LR B-spline basis $\mathbb{S}^{3,3}$

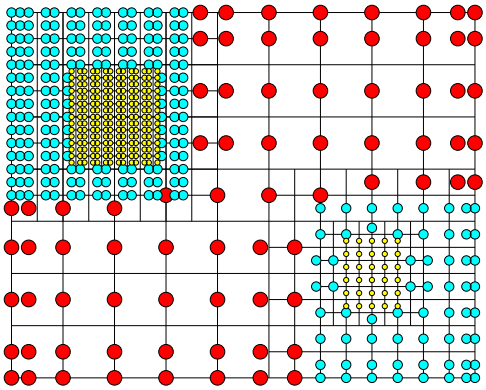

(b) LR B-spline basis $\mathbb{S}^{3,2}$

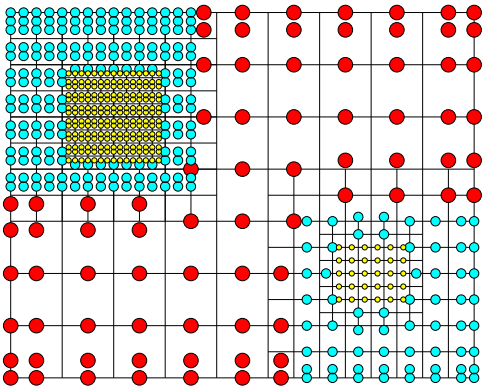

(c) LR B-spline basis $\mathbb{S}^{2,3}$

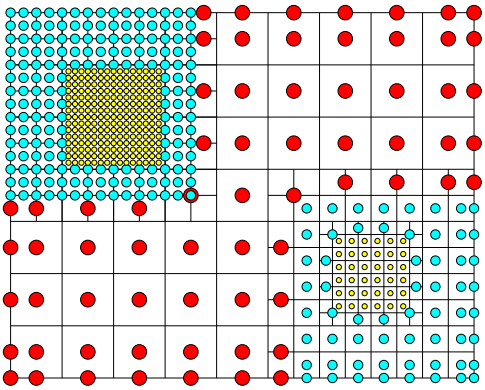

(d) LR B-spline basis $\mathbb{S}^{2,2}$

Figure 11: Example LR B-spline basis functions over a structured LR mesh $\mathcal{M}$. The functions are plotted at their Greville abscissa and colored according to the following rules: No yellow functions have support outside the finest elements, no teal functions have support on the largest elements and the functions represented in red color are the only ones having support on the largest elements.

6 Numerical results

In this section we present some numerical results to illustrate the performance of compatible LR B-splines discretization for solving the incompressible Stokes problem. The main focus is to show:

- Numerical stability of compatible LR B-spline discretizations
- Divergence free computed FE solution
- Efficiency and optimal convergence rate achieved by adaptive analysis.

In the numerical computation we consider three different choices of discrete spaces for the approximation of velocity and pressure fields in the mixed discretization (3) for Stokes problem. These choices of spline spaces, i.e, (V_h, Q_h), over a general box mesh $\mathcal{M}$ in the domain Ω are defined as:

$$\text{Type I} \quad : \quad V_h := X_h^1; \quad Q_h := X_h^2; \tag{32}$$

$$\text{Type II} \quad : \quad V_h := \{\mathbf{v} \in X_h^1, \quad \mathbf{v}\cdot\mathbf{n}|_{\partial\Omega} = 0\}; \tag{33}$$
$$Q_h := \{q \in X_h^2 : \int q = 0\};$$

$$\text{Type III} \quad : \quad V_h := \{\mathbf{v} \in X_h^1, \quad \mathbf{v}|_{\partial\Omega} = \mathbf{0}\}; \quad \text{and} \tag{34}$$
$$Q_h := \{q \in X_h^2 : \int q = 0 \quad \text{with} \quad q(\mathbf{x}_i) = 0, \quad i = 1, \ldots, 4\}.$$

with

$$X_h^1 = \mathbb{S}^{p+1,q}(\mathcal{M}) \times \mathbb{S}^{p,q+1}(\mathcal{M}) \text{ and } X_h^2 = \mathbb{S}^{p,q}(\mathcal{M});$$

where $\mathbb{S}^{p,q}_{k,\ell}(\mathcal{M})$ denotes the two-dimensional spline space of degree (p, q) and continuity (k, ℓ) in both directions, respectively, and $\mathbf{n}$ denotes the outward unit normal to the boundary of Ω and $\mathbf{x}_i, i = 1, ..., 4$ denote its four corners. In the numerical results presented in this section we always consider the case of equal degree approximation in both directions, i.e., $p = q$.
Error evaluation:

For our model Stokes problem, we distinguish between the velocity and pressure errors. We compute the error in velocity using the H^1 semi-norm defined by

$$|\boldsymbol{u} - \boldsymbol{u}_h|^2_{H^1(\Omega)} = \int_\Omega \nabla(\boldsymbol{u} - \boldsymbol{u}_h) : \nabla(\boldsymbol{u} - \boldsymbol{u}_h)\, d\Omega, \tag{35}$$

and the pressure error in L^2 norm;

$$\|p - p_h\|^2_{L^2(\Omega)} = \int_\Omega (p - p_h)^T \cdot (p - p_h) d\Omega. \tag{36}$$

For smooth problems, a div-compatible B-spline discretization is expected to satisfy:

$$\begin{aligned} |\boldsymbol{u} - \boldsymbol{u}_h|_{H^1} &= \mathcal{O}(h^s) \\ \|p - p_h\|_{L^2} &= \mathcal{O}(h^{s+1}) \end{aligned} \tag{37}$$

where s is the lowest polynomial degree in the approximation spaces pair of (V_h, Q_h), i.e., $s = \min(p, q)$, for the div-compatible LR discretization of $\boldsymbol{u}_h$ and p_h, and h is the radius of smallest circle encompassing the largest element in our discretization.

For locally refined adaptive meshes, we have a wide range of element sizes and it becomes misleading to measure the errors in terms of element size. We then reformulate the relations in (37) in terms of

degrees-of-freedom n_{dof}. By observing that a uniform mesh in two dimensions has $n_{\text{dof}} = \mathcal{O}(h^{-2})$, we state that the optimal rate of convergence, as measured against degrees of freedom is

$$\begin{aligned} |\boldsymbol{u} - \boldsymbol{u}_h|_{H^1} &= \mathcal{O}(n_{\text{dof}}^{-s/2}) \\ \|p - p_h\|_{L^2} &= \mathcal{O}(n_{\text{dof}}^{-(s+1)/2}). \end{aligned} \tag{38}$$

Whenever the exact solution is available, we define the error estimate η_F using a norm [1] per element (or face) F as

$$\eta_F^2 = \nu|\boldsymbol{u} - \boldsymbol{u}_h|_{H^1}^2 + \|p - p_h\|_{L^2}^2. \tag{39}$$

When summed over the entire domain we denote this as the total norm. The error contribution to each B-spline basis function η_B is defined as

$$\eta_B^2 = \sum_{F \in \text{supp}(B)} \eta_F^2. \tag{40}$$

Marking strategy

The marking strategy, that is, the method of how to choose the basis functions for refinement in structured mesh refinement is taken from [25], where once we have the value of estimated error at element level given by (40) (here elements is the same as face that we denote F) then we sum the element error on all elements within the support of each basis function. In the refinement strategies we always choose to refine a percentage of basis functions which contribute the most error. In [25], it was demonstrated that for a fixed percentage say $\beta = 5, 10, 20$ one achieved a proper adaptive refinement process resulting in optimal convergence rates. For the implementation in this article we always consider $\beta = 10$. In our refinement strategy, we always refine the LR B-spline basis functions of the potential space $\mathcal{S}^{p+1,q+1}(\mathcal{M})$ and then the construction of div-compatible LR B-spline spaces follows as we discussed in Section 5.

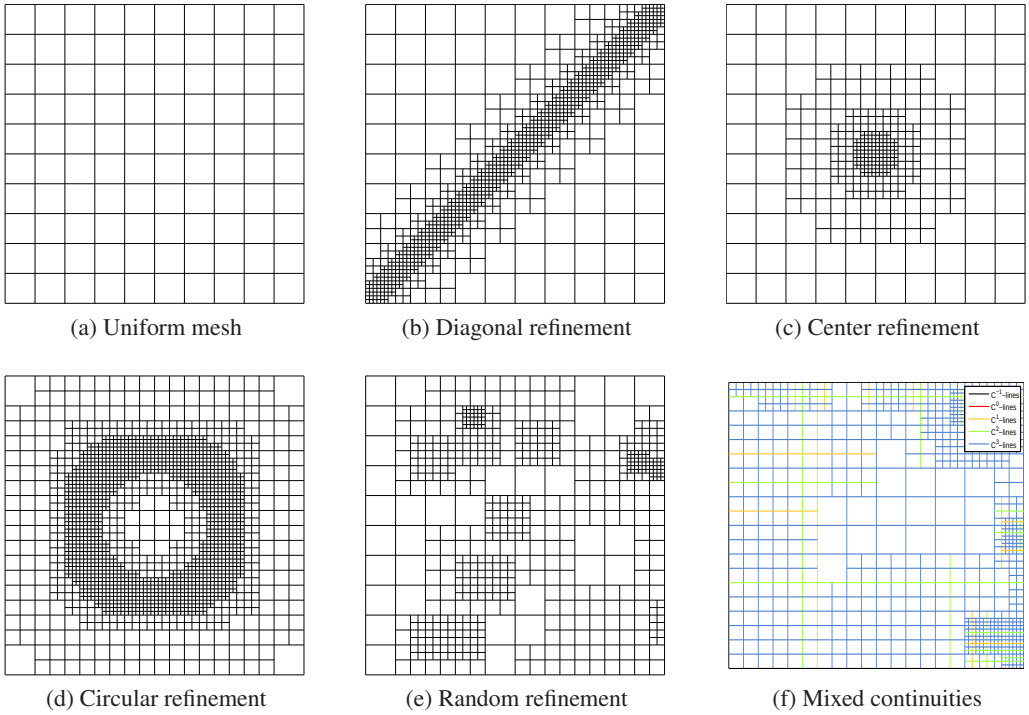

(a) Uniform mesh (b) Diagonal refinement (c) Center refinement

(d) Circular refinement (e) Random refinement (f) Mixed continuities

Figure 12: **Stability tests on Structured LR meshes:** LR meshes used for evaluation of the inf-sup constant. Note that the refinements (e)-(f) were computed randomly and as such differ between each simulation and discretization. The other meshes were computed algorithmically, and only depend on p.

6.1 Stability tests of Structured LR meshes

The performance of our methodology is based on the notion of Ladyženskaja-Babuška-Brezzi (LBB) condition, or the discrete inf-sup condition, cf. (4).

The different choices of discrete spaces (Q_h, V_h) as Type I, II, and III as defined above is considered on a set of *structured* LR meshes as shown in Figure 12. These meshes are constructed via some particular refinements (see Figures 12(a)-(d)) or randomly generated meshes (see Figures 12(e)-(f)), and represent the case of different compatible spline spaces of degrees p. Tables 1-3 show the computed values of inf-sup constant c_{is} with different choices of discrete spaces of Type I-III, respectively. It is confirmed from our computation in Tables 1-3 and Figure 13 that the inf-sup constant $c_{is} > 0$ and has large values.

p	Uniform	Diagonal	Center	Circle	Random	Mixed
1	0.9370	0.6535	0.6837	0.6802	0.5876	0.6606
2	0.9375	0.6098	0.6204	0.6459	0.6278	0.5873
3	0.8818	0.5378	0.8818	0.5295	0.5171	0.5401

Table 1: **Stability tests on Structured LR meshes:** Computed inf-sup constant c_{is} for Type I discretization without boundary conditions.

p	Uniform	Diagonal	Center	Circle	Random	Mixed
1	0.9306	0.6534	0.6837	0.6802	0.5842	0.6222
2	0.8912	0.6097	0.6204	0.6458	0.6117	0.5680
3	0.8240	0.5378	0.8240	0.5293	0.5810	0.5524

Table 2: **Stability tests on Structured LR meshes:** Computed inf-sup constant c_{is} for Type II discretization with no penetration boundary conditions $\boldsymbol{u} \cdot \boldsymbol{n} = 0$.

p	Uniform	Diagonal	Center	Circle	Random	Mixed
1	0.4591	0.4243	0.4592	0.4108	0.3540	0.3481
2	0.4908	0.4534	0.4908	0.4761	0.4447	0.2338
3	0.4833	0.4561	0.4833	0.4708	0.1387	0.3095

Table 3: **Stability tests on Structured LR meshes:** Computed inf-sup constant c_{is} for Type III discretization with no slip boundary conditions $\boldsymbol{u} = \boldsymbol{0}$.

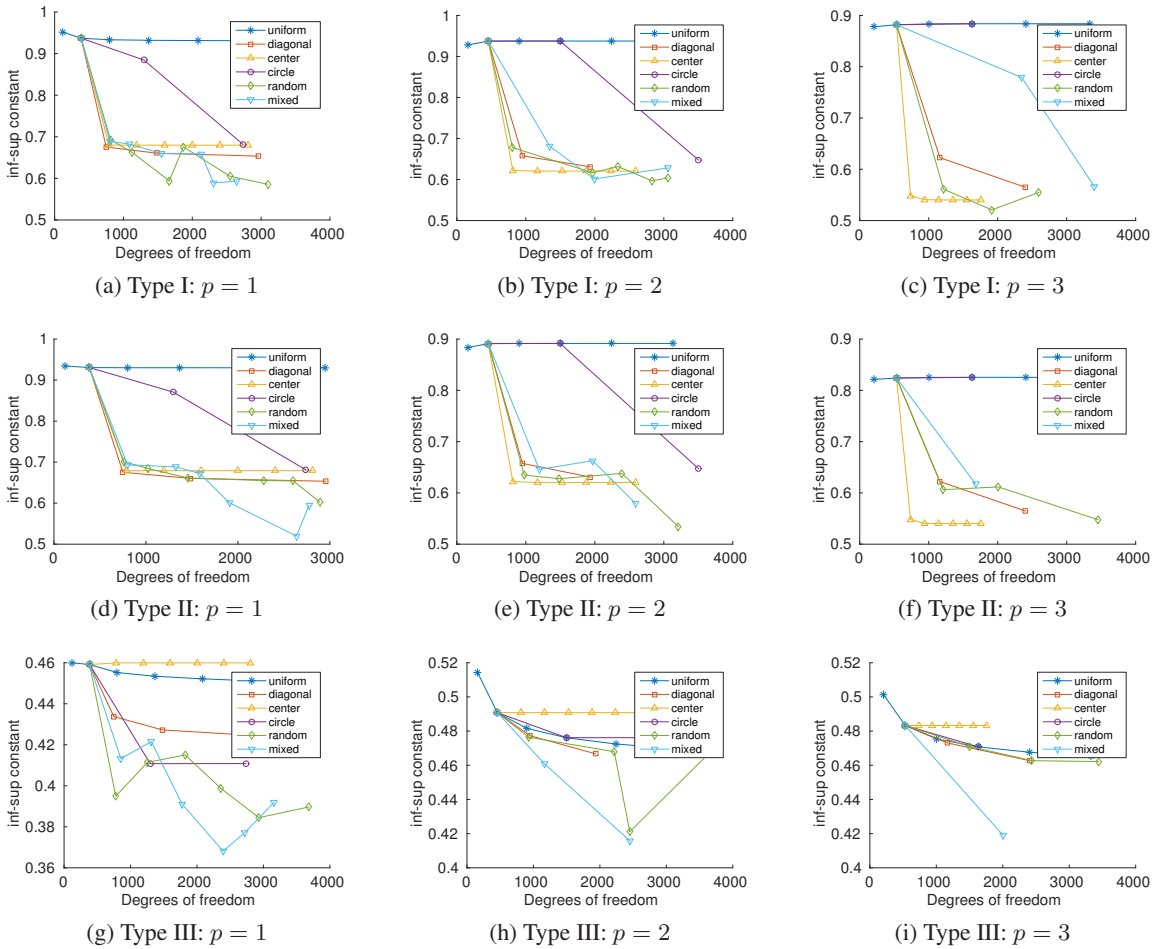

(a) Type I: $p = 1$ (b) Type I: $p = 2$ (c) Type I: $p = 3$

(d) Type II: $p = 1$ (e) Type II: $p = 2$ (f) Type II: $p = 3$

(g) Type III: $p = 1$ (h) Type III: $p = 2$ (i) Type III: $p = 3$

Figure 13: **Stability tests on Structured LR meshes:** Computed inf-sup constant on a series of meshes under refinement. Six different refinement strategies was studied, all shown in Figure 12. We have plotted the inf-sup constant c_{is} as a function of the degrees of freedom. We see that $c_{is} > 0$ is large for all cases studied here. With the exception of uniform refinement (which goes like $h_{\text{min}} = 1/n$), all mesh iterations are characterized by halving the smallest element between data points, i.e. $h_{\text{min}} = 1/2^n$.

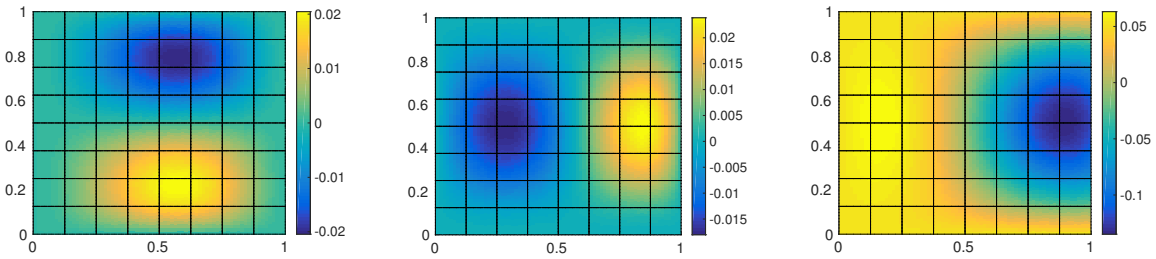

(a) Exact velocity x-component (b) Exact velocity y-component (c) Exact pressure

Figure 14: **Stokes problem with smooth solution:** The exact solution of the Stokes problem given in (41).

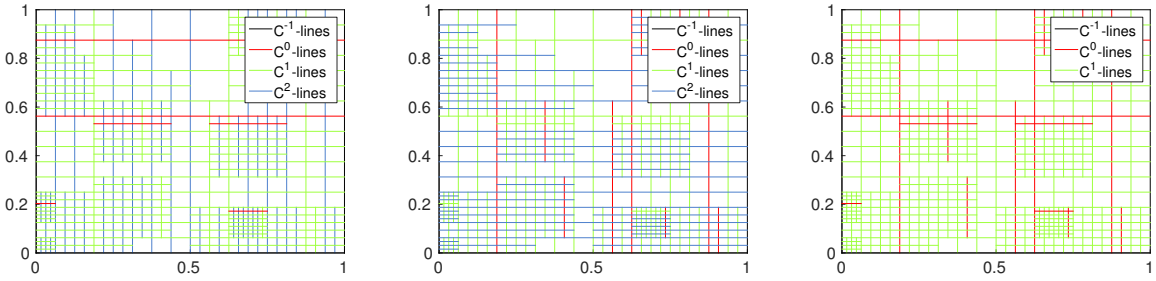

(a) $\mathbb{S}^{3,2}(\mathcal{M})$ for velocity x-component (b) $\mathbb{S}^{2,3}(\mathcal{M})$ for velocity y-component (c) $\mathbb{S}^{2,2}(\mathcal{M})$ for pressure

Figure 15: **Stokes problem with smooth solution:** Compatible LR B-splines approximation spaces for the velocity and pressure fields on the irregular LR mesh $\mathcal{M}$ with mixed continuities using LR B-splines.

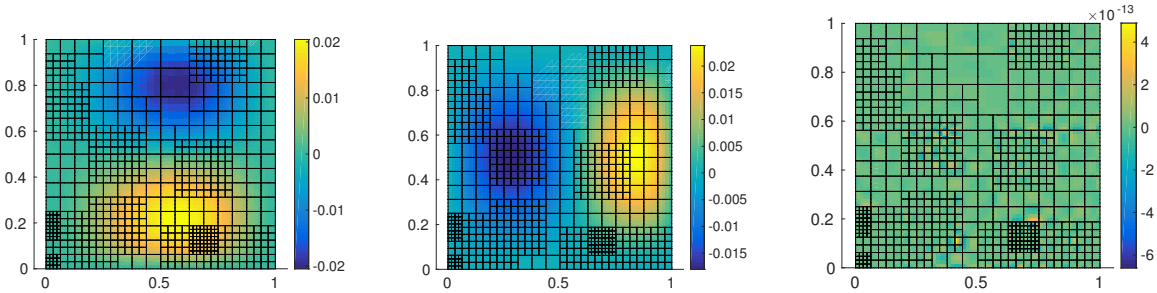

(a) Computed velocity x-component (b) Computed velocity y-component (c) Divergence of computed velocity

Figure 16: **Stokes problem with smooth solution:** Finite element solution of Stokes problem with smooth solution using LR B-spline compatible spaces on a (randomly generated) irregular LR mesh, with no-slip boundary conditions $\boldsymbol{u} = \mathbf{0}$. The LR B-spline compatible discretization shows pointwise divergence free solution up to machine precision.

6.2 Divergence free computed FE solution

Example 1: Stokes problem with smooth solution

We consider an example of Stokes problem with smooth solution on a square domain $\Omega = (0,1)^2$ with no-slip boundary conditions as presented in Buffa et al. [10]. The viscosity term is taken as $\nu = 1$ and **f** is constructed based on the exact solution given as:

$$\begin{aligned} \boldsymbol{u} &= \begin{bmatrix} 2e^x(x-1)^2x^2(y^2-y)(2y-1) \\ -e^x(x-1)x(-2+x(x+3))(y-1)^2y^2 \end{bmatrix} \\ p &= (-424+156e+(y^2-y)(-456+e^x(456+x^2(228-5(y^2-y)) \\ &\quad +2x(-228+(y^2-y))+2x^3(-36+(y^2-y))+x^4(12+(y^2-y)))). \end{aligned} \tag{41}$$

These exact solutions are depicted in Figure 14. We consider the Type III discretization to solve this problem with the choice of compatible LR B-spline spaces defined on irregular and randomly generated LR mesh in Figure 15. The computed FE solution using these compatible LR B-spline spaces are shown in Figure 16. It can be observed from the divergence of computed velocity field shown in Figure 16(c) that the LR B-spline compatible discretization gives pointwise divergence free solution up.

6.3 Optimal convergence rates

For the Type III choice of discrete spaces with tensor product B-splines, it has been pointed out [10] that the error in H^1-seminorm of the velocity will be of optimal order, i.e., $\mathcal{O}(h^p)$, whereas the error in L^2-norm of pressure is limited to linear convergence, regardless the polynomial degree of approximation spaces used. The results in Figure 17 show the same behavior in our FE computations for compatible B-splines spaces with uniform h-refinement for Stokes problem with smooth solution. The authors in [10] also proposed two solutions based on either augmenting the system by enforcing one component of the momentum to be zero at the corners or by using a particular case of T-splines, and their results show that both choices gave an optimal rate of convergence, i.e. $O(h^{p+1})$, for the pressure.

The reason for suboptimal convergence of the pressure is that we require this to be prescribed at the four corners as apparent from the choice of function space Z_h^2. Observe that the analytic solution given in (41) does not satisfy $p(x_i) = 0$ at the corner points x_i, and enforcing the approximated pressure p_h wrongly to zero is the cause of linear convergence. Strongly enforcing the pressure to the correct value gives optimal convergence, but it is not customary to know this value a priori.

Several "tricks" may be applied to remedy this, including the two mentioned by [10]. For the purpose of this work we propose a conceptual simple solution which proves effective. This is simply done by setting the pressure to zero at the corners and refine away all problems arising from this. Mathematically one may think of it like this. By setting the pressure (wrongly) to zero, one is introducing an artificial singularity around these points, and we may resolve this singularity by local refinement.

The error plots results presented in Figure 18 show that an optimal rate of convergence is achieved via adaptive refinements, i.e., $O(h^{p+1})$ for L^2-norm of the pressure and $O(h^p)$ for the total norm of the solution. The LR meshes obtained at different steps of adaptive refinements are given in Figure 19.

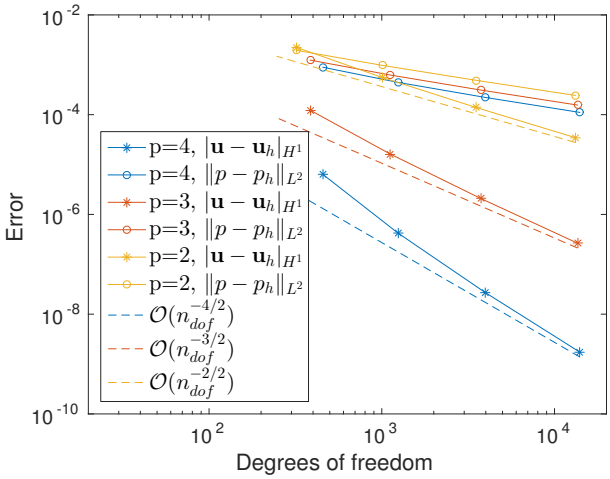

Figure 17: **Stokes problem with smooth solution:** Convergence rates for compatible spline discretization with the choice of Type III discrete spaces. The error in L^2-norm of pressure shows only linear convergence rates, regardless of polynomial degree of discretization, while the error in velocity achieve optimal rates.

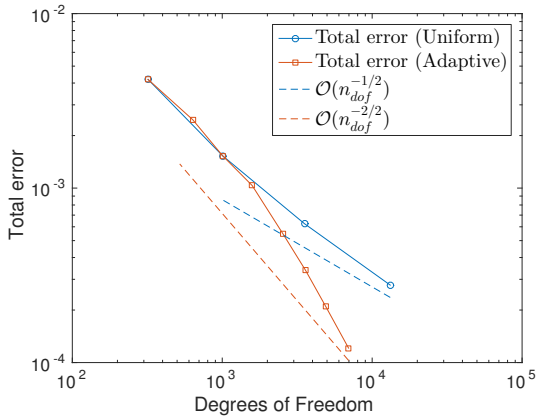

(a) Convergence in total norm for $p = 2$

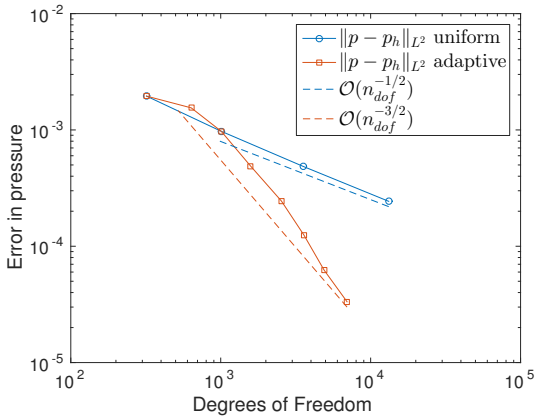

(b) Convergence in p_h for $p = 2$

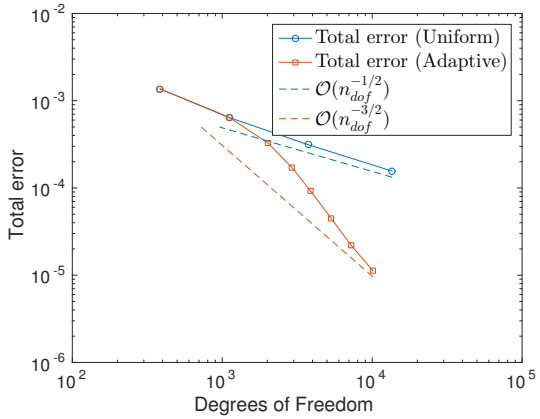

(c) Convergence in total norm for $p = 3$

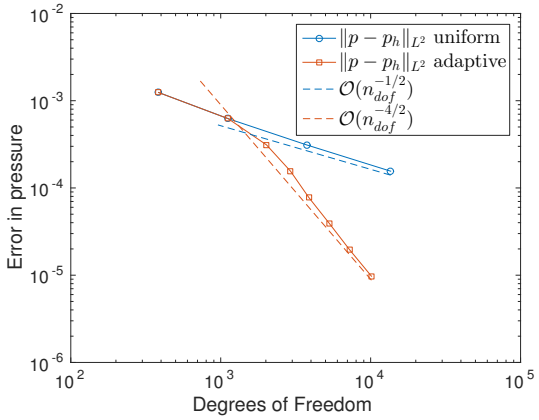

(d) Convergence in p_h for $p = 3$

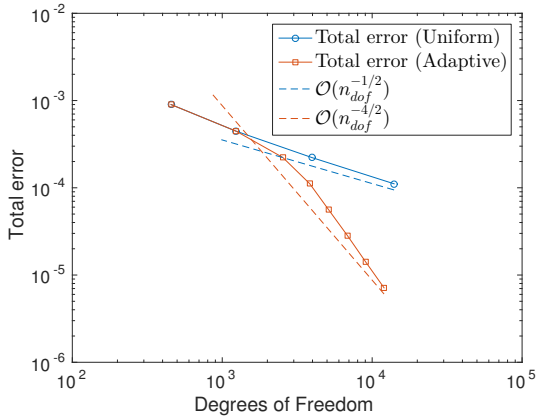

(e) Convergence in total norm for $p = 4$

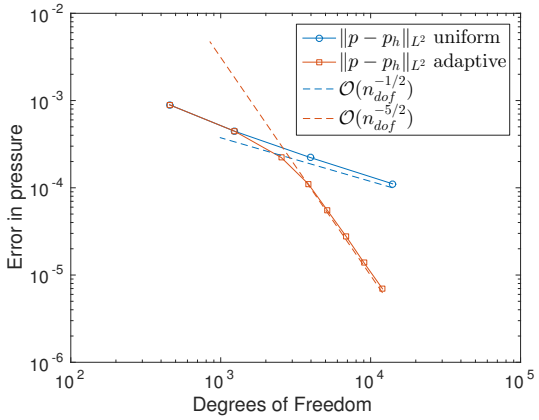

(f) Convergence in p_h for $p = 4$

Figure 18: **Stokes problem with smooth solution:** Convergence rates for adaptive compatible LR spline discretization with the choice of Type III discrete spaces based on exact total error. The total error $\nu|\mathbf{u} - \mathbf{u}_h|_{H^1} + \|p - p_h\|_{L^2}$ and pressure error shows optimal rate of convergence.

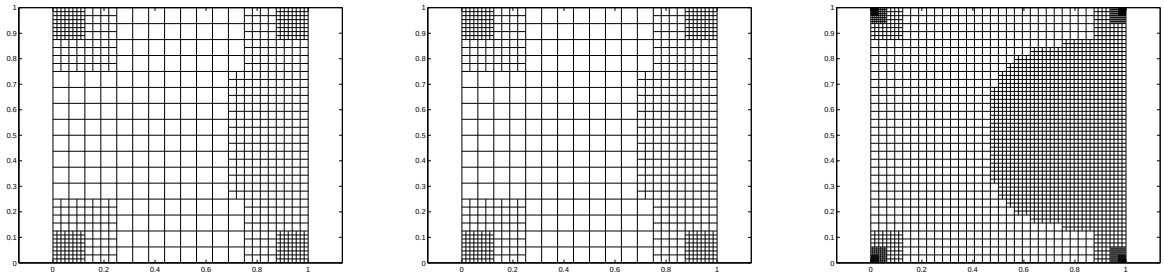

(a) 3rd iteration for $p = 2$ (b) 5th iteration for $p = 2$ (c) 9th iteration for $p = 2$

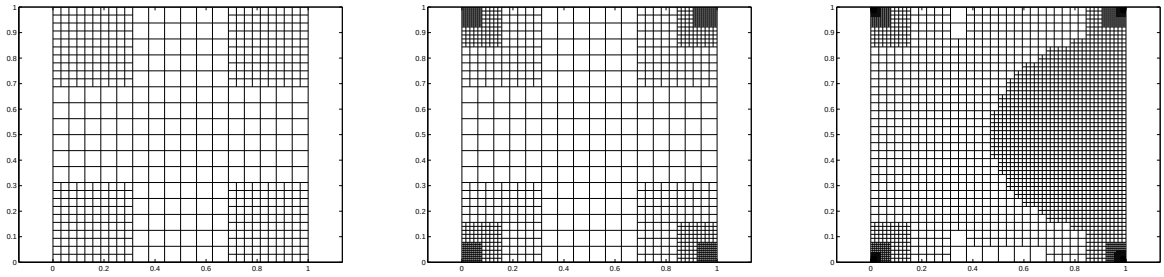

(d) 3rd iteration for $p = 3$ (e) 5th iteration for $p = 3$ (f) 9th iteration for $p = 3$

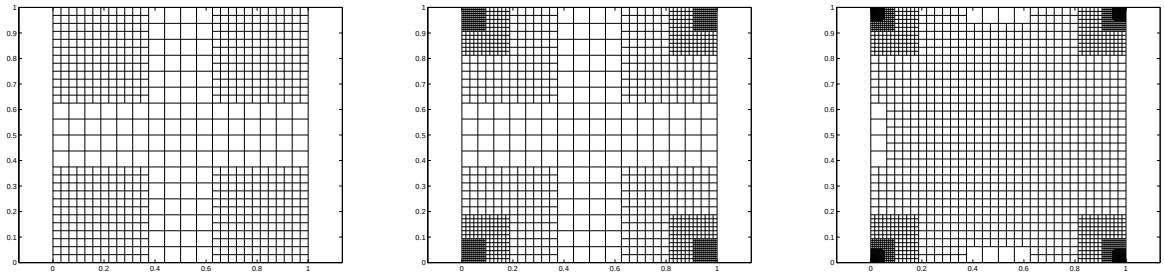

(g) 3rd iteration for $p = 4$ (h) 5th iteration for $p = 4$ (i) 9th iteration for $p = 4$

Figure 19: **Stokes problem with smooth solution:** The LR meshes obtained via adaptive refinements using compatible LR B-splines with Type III discrete setting. As the polynomial degree increases, the discrepancy between pressure error and velocity error for uniform meshes increases. Thus, for higher polynomial degrees the error in the pressure is dominant, resulting in more refinement at the corners.

6.4 The benchmark problem: Lid-driven cavity flow

In this section, we investigate the effectiveness of our methodology for a benchmark case of incompressible flows: two-dimensional lid driven cavity problem. The problem setup is a square domain $\Omega = (0,1)^2$ with fixed no-slip boundary conditions on the left, right and bottom side of the domain, with a prescribed velocity $\boldsymbol{u} = [1,0]$ in positive horizontal direction (i.e. to the right) on the top edge. This is illustrated in Figure 20. The viscosity constant is taken as $\nu = 1$ and the force $\mathbf{f}$ is defined as zero. The problem setup is known to induce failures in unstable formulations due to the pressure singularities at both top corners of the domain, while in some particular region of interest around both lower corners an infinite series of recirculation regions appears.

Since the boundary conditions are discontinuous, we cannot exactly represent them in our function space, but we impose them in a "leaky" fashion by setting all control points corresponding to the x-velocity at the top to one, including the two corners. The rest of the boundary velocity control points are set to zero. This results in a very small, but nonzero region on both the left and right edge where we have velocity components in the x-direction. This region will decrease under refinement as the support of the corner control points diminishes, and will in the limit approach discontinuous.

The exact solution for the lid driven cavity problem is not known, so we decide to locally refined the LR mesh at all the four corners by hand. The local refinement at the two corners at the top is introduced to suppress the pollution effect of the singularities in the pressure field at those points. The refinement at the two lower corners are introduced to resolve the recirculation zone with high accuracy. The first four hand made locally refined LR meshes are given in Figure 23. To solve the lid driven cavity problem, we consider the Type III pair of discrete approximation spaces on these LR meshes where a no-slip condition is imposed on all sides of the domain for velocity field, with the exception of prescribed velocity at the top which is enforced strongly; and zero average pressure with additional four constraints to force the pressure value to zero at the corner. The computed FE solutions, i.e., the component of velocity and pressure with the divergence of computed velocity field, i.e., $\text{div}(\mathbf{u}_h)$ are shown in Figure 21. The computed solution displays pointwise divergence free solution (up to machine precision) with no spurious oscillations in Figure 21, whereas the velocity profiles across the center (horizontal and vertical direction) are shown in Figure 24.

The streamlines plots of the computed velocity field $\boldsymbol{u}_h$ are shown in Figure 25a. Due to the presence of local refinement at the bottom corners we observe three *moffat eddies* in our computed FE solution, even for relatively low degrees of freedom. In our FE-discretization used to compute the streamline plots displayed in Figure 25, we consider $(p,q) = (1,1)$ and $n_{dof} = 3649$ for the pressure field, and $(p,q) = (1,2) \times (2,1), n_{dof} = 7332$ for the velocity fields.

To illustrate the performance our methodology for the lid cavity driven problem, we consider to compare the *curl* of our computed FE solution at the point $\boldsymbol{x} = (1, 0.95)$ to available results in literature. The value of the curl of our computed solution at $(1, 0.95)$ using the compatible LR B-spline discretization with uniform and adaptive refinement, along with two available reference solutions in literature, see [20, 9], are shown in Tables 4–7 for Type III pair of discrete spaces of degrees, $p = 1, 2, 3, 4$, respectively. Since our formulation in this paper are based on strong enforcement of the boundary conditions and in Type III pairing of spaces we enforced the pressure at the top corner points to zero that causes the singularities in the solution. This degrades the convergence in the pressure error and hence produce worse results for uniform refinement than those tabulated in [20]. However, our adaptive methodology using local refinement is able to compensate after some iterations. From the results presented in Tables 4–7 the convergence in adaptive refinement can be noticed and as the value of p increases the *curl* value of the computed solution quickly approach the reference value as given by using Pseduspectral method of [9]. While if we compare our adaptive results with the uniform refinement results of Evans [20] then the efficiency achieved by our adaptive methodology in term of degrees of freedom is clearly noticeable.

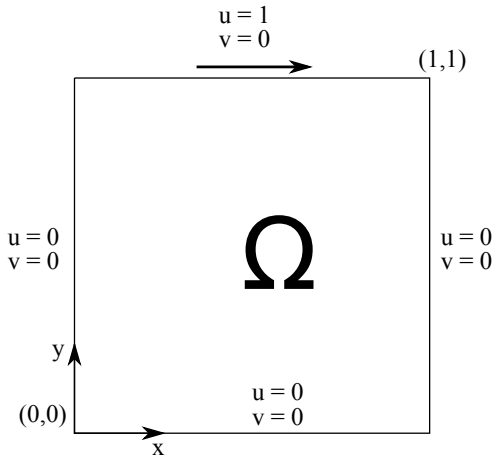

Figure 20: **Lid-driven cavity:** Problem setup for the lid-driven cavity flow.

Present method	$h_{\min}$	$h_{\max}$	n_{dof}	ω
Uniform B-spline	1/16	1/16	764	-14.6690
Uniform B-spline	1/32	1/32	3 068	7.6529
Uniform B-spline	1/64	1/64	12 284	15.2317
Adaptive step #1	1/32	1/16	1 676	7.6529
Adaptive step #2	1/64	1/16	2 588	15.2310
Adaptive step #3	1/128	1/16	3 500	20.7713
Adaptive step #4	1/256	1/16	4 412	22.5232
Adaptive step #5	1/512	1/16	5 324	23.2820
Adaptive step #6	1/1024	1/16	6 236	23.6602
Adaptive step #7	1/2048	1/16	7 148	23.8492
Adaptive step #8	1/4096	1/16	8 060	23.9436
Spline disct.(Ref. [20])	1/64	1/64	12 804	19.0446
Spline disct.(Ref. [20])	1/256	1/256	198 660	25.3224
Pseudospectral (Ref. [9])	-	-	-	27.2790

Table 4: **Lid-driven cavity flow:** Computed values for $\omega = \text{curl}(\boldsymbol{u}_h)$ at the point $\boldsymbol{x} = (1, 0.95)$ for $p = 1$.

The difference in number of degrees of freedom for the case of uniform refinement between the present study and the one reported in [20] is due to strong and weak enforcement of of the Dirichlet boundary conditions, respectively.

Present method	$h_{\min}$	$h_{\max}$	n_{dof}	ω
Uniform B-spline	1/16	1/16	863	-0.2911
Uniform B-spline	1/32	1/32	3 263	17.8810
Uniform B-spline	1/64	1/64	12 671	23.5541
Adaptive step #1	1/32	1/16	1 775	17.8810
Adaptive step #2	1/64	1/16	2 687	23.5540
Adaptive step #3	1/128	1/16	3 599	25.3342
Adaptive step #4	1/256	1/16	4 511	26.3943
Adaptive step #5	1/512	1/16	5 423	26.9274
Adaptive step #6	1/1024	1/16	6 335	27.1947
Adaptive step #7	1/2048	1/16	7 247	27.3283
Adaptive step #8	1/4096	1/16	8 159	27.3951
Spline disct.(Ref. [20])	1/64	1/64	13 199	32.8197
Spline disct.(Ref. [20])	1/256	1/256	200 207	27.3440
Pseudospectral (Ref. [9])	-	-	-	27.2790

Table 5: **Lid-driven cavity flow:** Computed values for $\omega = \text{curl}(\boldsymbol{u}_h)$ at the point $\boldsymbol{x} = (1, 0.95)$ for $p = 2$.

Present method	$h_{\min}$	$h_{\max}$	n_{dof}	ω
Uniform B-spline	1/16	1/16	968	10.9593
Uniform B-spline	1/32	1/32	3 464	22.1396
Uniform B-spline	1/64	1/64	13 064	24.6936
Adaptive step #1	1/32	1/16	1 880	22.1396
Adaptive step #2	1/64	1/16	2 792	24.6937
Adaptive step #3	1/128	1/16	3 704	25.7774
Adaptive step #4	1/256	1/16	4 616	26.5183
Adaptive step #5	1/512	1/16	5 528	26.9092
Adaptive step #6	1/1024	1/16	6 440	27.1048
Adaptive step #7	1/2048	1/16	7 352	27.2025
Adaptive step #8	1/4096	1/16	8 264	27.2514
Spline disct.(Ref. [20])	1/64	1/64	13 600	29.9294
Spline disct.(Ref. [20])	1/256	1/256	201 760	27.5264
Pseudospectral (Ref. [9])	-	-	-	27.2790

Table 6: **Lid-driven cavity flow:** Computed values for $\omega = \text{curl}(\boldsymbol{u}_h)$ at the point $\boldsymbol{x} = (1, 0.95)$ for $p = 3$.

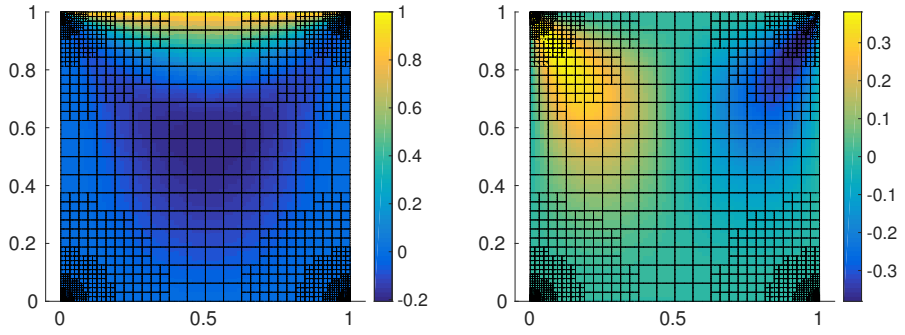

(a) First component of the velocity $\boldsymbol{u}_h$

(b) Second component of the velocity $\boldsymbol{u}_h$

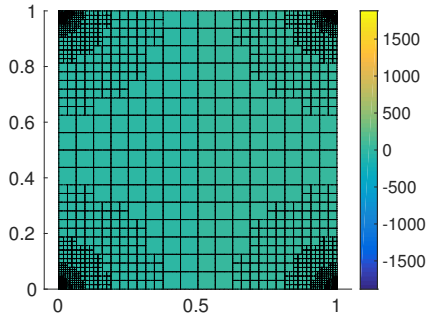

(c) Pressure solution p_h

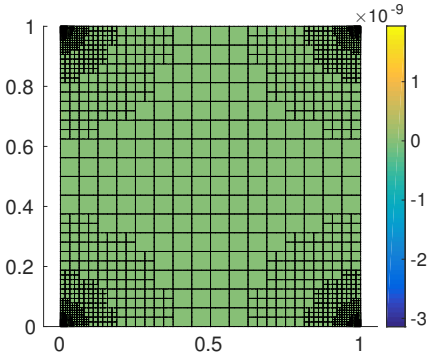

(d) div$(\boldsymbol{u}_h)$

Figure 21: **Lid-driven cavity flow:** FE solution plot of the computed velocity, pressure and divergence. This is the fifth iteration using polynomial degree $(p, q) = (2, 2)$ for the pressure and $(3, 2) \times (2, 3)$ for the velocity.

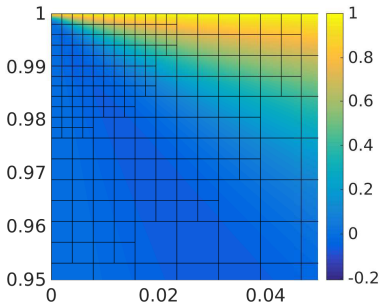

(a) First component of the velocity $\boldsymbol{u}_h$

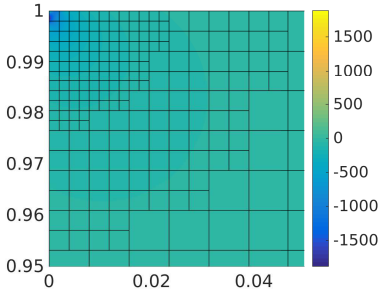

(b) Pressure solution p_h

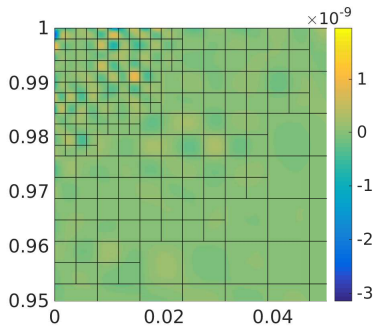

(c) div$(\boldsymbol{u}_h)$

Figure 22: **Lid-driven cavity flow:** Details regarding the top left corner on the results from Figure 21. **(a)** The discontinuous boundary conditions are implemented in a "leaky" fashion by setting all control points at the top, including the corner one to the value 1. The rest are kept at 0. **(b)** The true solution has a large negative pressure at the corner point. Since we don't know this a priori and the space Z_h^2 requires us to prescribe it, we are setting p_h to zero at the corner. This error is localized by the local refinement. **(c)** Numerical round-off is amplified when using local refinement and is most pronounced at finer regions, hence we do not see $\mathcal{O}(10^{-15})$ in evaluation. Analytical expressions yield pointwise zero divergence everywhere.

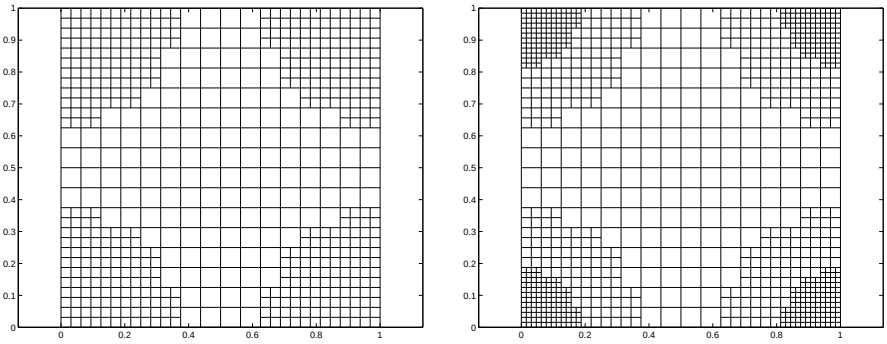

(a) First refinement (b) Second refinement

(c) Third refinement (d) Fourth refinement

Figure 23: **Lid-driven cavity flow:** The hand-made adaptive mesh refinement used to solve the Lid-driven cavity problem. For each iteration, we refine every B-spline completely contained within a $6.5 \cdot 2^{-4-i}$ radius of each corner.

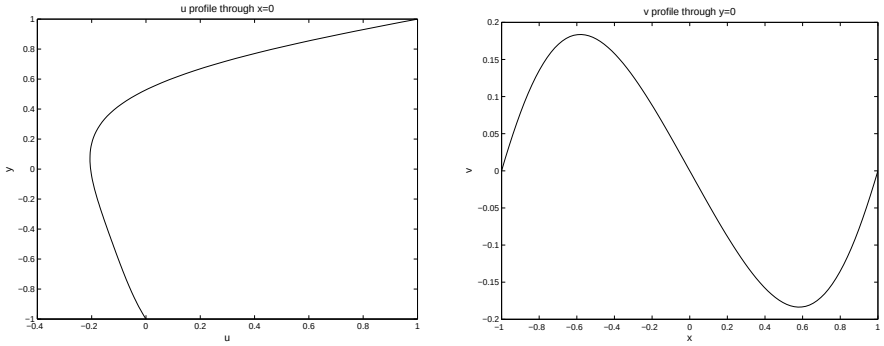

(a) Values of the first velocity component at a vertical line through the center

(b) Values of the second velocity component at a horizontal line through the center

Figure 24: **Lid-driven cavity flow:** Velocity profiles across the center of the domain.

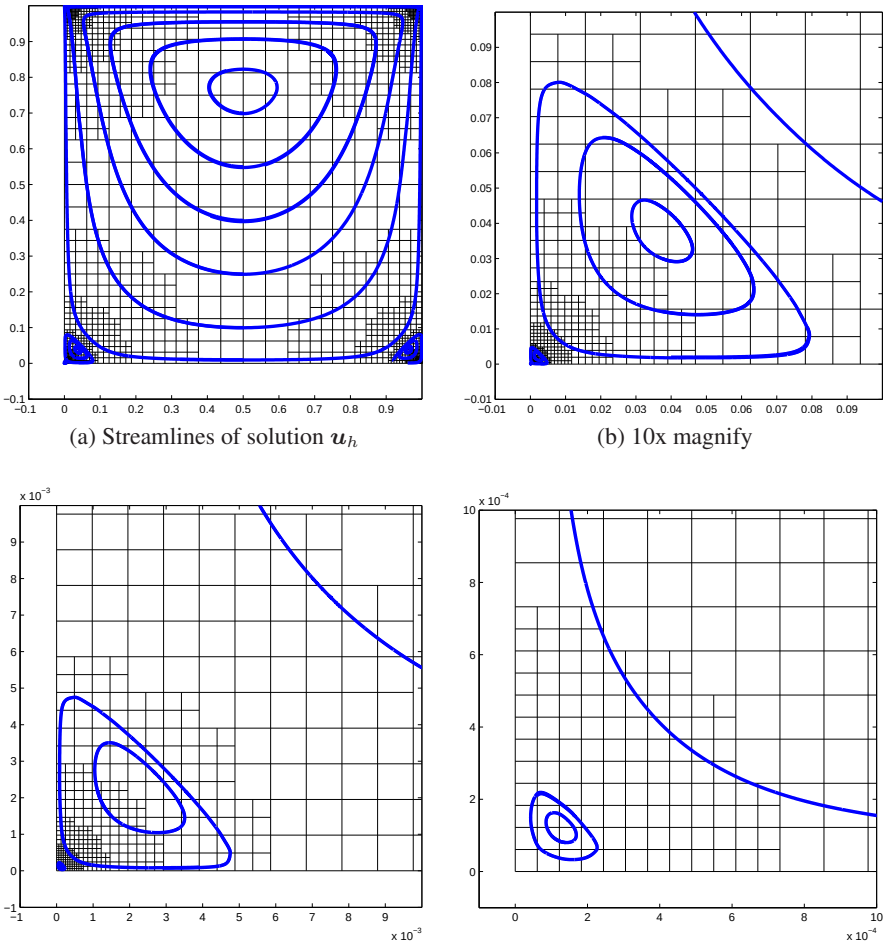

(a) Streamlines of solution $\boldsymbol{u}_h$

(b) 10x magnify

(c) 100x magnify

(d) 1000x magnify

Figure 25: **Lid-driven cavity flow:** Streamlines of the solution $\boldsymbol{u}_h$. We achieve pointwise divergent free solution (up to machine precision) using Type III discrete spaces. By refining around the corners we observe three moffatt eddies around the corners, even for relatively low degrees of freedom. The discretization shown here is $(p, q) = (1, 1)$ and $n = 3649$ for the pressure, and $(p, q) = (1, 2) \times (2, 1), n = 7332$ for the velocity.

Present method	$h_{\min}$	$h_{\max}$	n_{dof}	ω
Uniform B-spline	1/16	1/16	1 079	17.9896
Uniform B-spline	1/32	1/32	3 671	22.1748
Uniform B-spline	1/64	1/64	13 463	23.7481
Adaptive step #1	1/32	1/16	1 991	22.1745
Adaptive step #2	1/64	1/16	2 903	23.7487
Adaptive step #3	1/128	1/16	3 815	26.5231
Adaptive step #4	1/256	1/16	4 727	26.6432
Adaptive step #5	1/512	1/16	5 639	26.9621
Adaptive step #6	1/1024	1/16	6 551	27.1183
Adaptive step #7	1/2048	1/16	7 463	27.1964
Adaptive step #8	1/4096	1/16	8 375	27.2354
Pseudospectral (Ref. [9])	-	-	-	27.2790

Table 7: **Lid-driven cavity flow:** Computed values for $\omega = \text{curl}(\boldsymbol{u}_h)$ at the point $\boldsymbol{x} = (1, 0.95)$ for $p = 4$.

7 Conclusions

The aim of this paper has been to take the first step in the direction of extending the previous work on div-compatible spaces by Buffa *et al.* [10, 11] and Evans [20] to finite element analysis using LR B-splines. Herein, we have developed the methodology for making div-compatible LR B-spline spaces, i.e. which form complete De Rham complexes. These are stable, pointwise divergent free and facilitate local refinement capabilities. The numerical tests demonstrate significant improvements in accuracy per degree of freedom when solving Stokes problems.

No-slip discretizations are challenging as they require the pressure to be specified in the corners. These will typically require special treatment or we will loose convergence properties. We show that it is possible to set the corner values of the pressure to zero and "refine away" any problems arising from this making it possible to use the strong formulation for no-slip problems. This methodology is conceptually simple and still produces a compatible pointwise divergent free solution which shows optimal convergence in both pressure and velocity.

We have shown that the properties of compatible space discretization carry over from tensor product analysis to locally refined meshes.

The authors consider the following topics suited for future work in this field:

- Develop a closed expression for the pressure at the four corner points, only dependent on a prescribed slip $\boldsymbol{u} = \boldsymbol{g}$ on the boundary and the source term $\boldsymbol{f}$ in the interior.
- Include divergence-conforming mappings to handle realistic physical domains [10].
- Consider multiple patches or non-rectangular parametric domains for more complex geometries.
- Enable the use of weakly enforced boundary conditions [20].
- Extend to 3D by the use of the dimensional formula of Pettersen [31].
- Develop suitable error estimates for Stokes and Navier-Stokes flows.
- Investigate the applications of compatible discretization in electromagnetic differential equations [13].
- Show that the Hierarchical B-splines also satisfy the dimensional formula [28] and can be applied in the same framework.

8 Acknowledgement

The authors gratefully acknowledge the the financial support from the Norwegian Research Council and the industrial partners of the ICADA project (Ceetron, DNV GL and Statoil) and the FME NOWITECH (www.nowitech.no). They also acknowledge the support from the other co-workers in the IFEM software team.

A On the potential function in compatible space discretization

In this paper, we construct compatible spaces and show that they form a complete de Rham complex. We collect these results in Theorem 2, 3 and 4. Seeing as these theorems are considered the main results of the paper, we would like to elaborate on a specific part. During the proof, we say that

$$\mathrm{im}(\mathbf{rot}) = \ker(\mathrm{div}) \tag{42}$$

for the sequence $\mathbb{R} \to X_h^0 \to X_h^1 \to X_h^2 \to 0$, $0 \to Y_h^0 \to Y_h^1 \to Y_h^2 \to 0$ and $0 \to Z_h^0 \to Z_h^1 \to Z_h^2 \to 0$.

This can be shown by proving that any potential field has a divergence-free velocity, and any divergence-free velocity has a potential field. Written more formally, we say that

$$\forall \varphi \in X_h^0 \quad \exists \quad \boldsymbol{u} \in X_h^1 : \mathbf{rot}(\varphi) = \boldsymbol{u} \wedge \mathrm{div}(\boldsymbol{u}) = 0 \tag{43}$$

$$\forall \boldsymbol{u} \in X_h^1 : \mathrm{div}(\boldsymbol{u}) = 0 \quad \exists \quad \varphi \in X_h^0 : \mathbf{rot}(\varphi) = \boldsymbol{u} \tag{44}$$

and likewise for the spaces with boundary conditions, i.e. Y_h and Z_h.

A.1 Proving im(rot)⊆ker(div)

First note that any potential field maps to a divergence-free space under the **rot** operator

$$\mathrm{div}(\mathbf{rot}(\varphi)) = \mathrm{div}\left(\begin{bmatrix} \frac{\partial \varphi}{\partial y} \\ -\frac{\partial \varphi}{\partial x} \end{bmatrix}\right) = \frac{\partial^2 \varphi}{\partial x \partial y} - \frac{\partial^2 \varphi}{\partial x \partial y} = 0. \tag{45}$$

$$\mathbf{rot}(\varphi) = \begin{bmatrix} \frac{\partial \varphi}{\partial y} \\ -\frac{\partial \varphi}{\partial x} \end{bmatrix} = \begin{bmatrix} u_1 \\ u_2 \end{bmatrix} \tag{46}$$

By considering spaces of boundary conditions, we will also need to check if these are satisfied under mapping. First consider a $\varphi \in Y_h^0$. As $\varphi = 0$ along the edges, we have that the tangential derivative along the edge is zero. That is $\frac{\partial \varphi}{\partial x} = -u_2 = 0$ on the top and bottom edge, while $\frac{\partial \varphi}{\partial y} = u_1 = 0$ on the left and right edge. Hence $\mathbf{rot}(\varphi) \in Y_h^1$.

For any $\varphi \in Z_h^0$ we have that both the normal and tangential derivative along the edge is zero, i.e. $\frac{\partial \varphi}{\partial x} = \frac{\partial \varphi}{\partial y} = 0$ on all edges. Hence $\boldsymbol{u} = \mathbf{0}$ on the boundary and $\mathbf{rot}(\varphi) \in Z_h^1$.

A.2 Proving im(rot)⊇ker(div)

Assume we have $\boldsymbol{u} \in X_h^0$, such that $\mathrm{div}(\boldsymbol{u}) = 0$. We then want to construct a potential field φ such that $\mathbf{rot}(\varphi) = \boldsymbol{u}$. This can be formalized as

$$\frac{\partial \varphi}{\partial y} = u_1(x, y) \tag{47}$$

$$\frac{\partial \varphi}{\partial x} = -u_2(x, y). \tag{48}$$

We integrate the first line to get

$$\varphi(x, y) = \int_a^y u_1(x, t)\ dt + C(x) \tag{49}$$

which differentiated with x becomes

$$\frac{\partial \varphi}{\partial x} = \int_a^y \partial_x u_1(x, t)\ dt + \partial_x C(x). \tag{50}$$

Setting in (48) yields

$$\begin{aligned}
-u_2(x,y) &= \int_a^y \partial_x u_1(x,t)\ dt + \partial_x C(x) \\
\partial_x C(x) &= -u_2(x,y) - \int_a^y \partial_x u_1(x,t)\ dt \\
\partial_x C(x) &= -u_2(x,y) - \int_a^y \partial_x u_1(x,t) + \partial_y u_2(x,t) - \partial_y u_2(x,t)\ dt \\
\partial_x C(x) &= -u_2(x,y) + \int_a^y \partial_y u_2(x,t)\ dt \\
\partial_x C(x) &= -u_2(x,y) + u_2(x,y) - u_2(x,a) \\
\partial_x C(x) &= -u_2(x,a) \\
C(x) &= -\int_b^x u_2(y,a)\ dt + c
\end{aligned} \tag{51}$$

where we have used that $\mathrm{div}(\boldsymbol{u}(x,t)) = \partial_x u_1(x,t) + \partial_y u_2(x,t) = 0$. By setting the constants all to zero, i.e. $a = b = c = 0$ and combining (49) and (51) we arrive at the potential field presented in the paper

$$\varphi(x,y) = \int_0^y u_1(x,t)\ dt - \int_0^x u_2(t,0)\ dt \tag{52}$$

and it can be checked that this satisfies $\mathbf{rot}(\varphi) = \boldsymbol{u}$.

A.2.1 The no penetration spaces Y_h

The very same function will work under spaces with boundary conditions as well, but may be simplified. Note that both Y_h^1 and Z_h^1 consists of functions, which second component vanishes at the bottom edge, i.e. $u_2(t,0) = 0$. For these spaces it is enough to consider the potential function

$$\varphi(x,y) = \int_0^y u_1(x,t)\ dt. \tag{53}$$

We show that this potential satisfies all boundary conditions, since we have from the derivations above that $\mathbf{rot}(\varphi) = \boldsymbol{u}$. Assuming the unit domain $\Omega = [0,1]^2$ we have for any $\boldsymbol{u} \in Y_h^1$

$$\begin{aligned}
u_1(0,y) &= 0 \\
u_1(1,y) &= 0 \\
u_2(x,0) &= 0 \\
u_2(x,1) &= 0
\end{aligned}$$

which in turn gives

$$\begin{aligned}
\varphi(0,y) &= \int_0^y u_1(0,t)\ dt = 0 \\
\varphi(1,y) &= \int_0^y u_1(1,t)\ dt = 0 \\
\varphi(x,0) &= \int_0^0 u_1(x,t)\ dt = 0 \\
\varphi(x,1) &= \int_0^1 u_1(x,t)\ dt.
\end{aligned}$$

The first two integrals equals to zero due to the boundary conditions on $\boldsymbol{u}$, while the third term is zero since the integration range is zero. The final term is also zero, but the reason is a little more subtle. For any given x, consider the closed line integral containing the subdomain $D = [0, x] \times [0, 1]$, i.e.

$$\begin{aligned}\oint \boldsymbol{u} \cdot \hat{\boldsymbol{n}}\, dS &= \int_0^1 u_1(x,t)\, dt + \\ &\int_x^0 u_2(t,1)\, dt + \\ &\int_1^0 -u_1(0,t)\, dt + \\ &\int_0^x -u_2(t,0)\, dt.\end{aligned}$$

Of the four right hand side integrals, only the first one does not immediately vanish as the three other are along boundary curves and have zero contribution due to $\boldsymbol{u} \in Y_h^0$. By using the divergence theorem we have that the left hand side integral is zero

$$\oint \boldsymbol{u} \cdot \hat{\boldsymbol{n}}\, dS = \iint_D \text{div}(\boldsymbol{u})\, dA = 0.$$

We are left with $\int_0^1 u_1(x,t)\, dt = 0$ which proves that $\varphi(x, y) = 0$ on all edges and hence $\varphi \in Y_h^0$.

A.2.2 The no slip spaces Z_h

The no slip spaces are conceptually no different than the no penetration spaces, but we include them here for completeness. The boundary conditions on Z_h^1 state

$$\begin{aligned}u_1(0,y) = \quad u_2(0,y) \quad &= 0 \\ u_1(1,y) = \quad u_2(1,y) \quad &= 0 \\ u_1(x,0) = \quad u_2(x,0) \quad &= 0 \\ u_1(x,1) = \quad u_2(x,1) \quad &= 0\end{aligned}$$

and we need to show that the generated φ satisfies the boundary conditions on Z_h^0 which states

$$\begin{aligned}\varphi(0,y) = \quad \tfrac{\partial\varphi}{\partial x}(0,y) \quad &= 0 \\ \varphi(1,y) = \quad \tfrac{\partial\varphi}{\partial x}(1,y) \quad &= 0 \\ \varphi(x,0) = \quad \tfrac{\partial\varphi}{\partial y}(x,0) \quad &= 0 \\ \varphi(x,1) = \quad \tfrac{\partial\varphi}{\partial y}(x,1) \quad &= 0.\end{aligned}$$

The conditions that $\varphi = 0$ on the boundary is analog to the previous section, and we now show that the normal derivative is also zero. We first remember that $\frac{\partial\varphi}{\partial x} = -u_2(x,y)$ and $\frac{\partial\varphi}{\partial y} = u_1(x,y)$, which means

$$\begin{aligned}\frac{\partial\varphi}{\partial x}(0,y) = \quad -u_2(0,y) \quad &= 0 \\ \frac{\partial\varphi}{\partial x}(1,y) = \quad -u_2(1,y) \quad &= 0 \\ \frac{\partial\varphi}{\partial y}(x,0) = \quad u_1(x,0) \quad &= 0 \\ \frac{\partial\varphi}{\partial y}(x,1) = \quad u_1(x,1) \quad &= 0.\end{aligned}$$

We conclude that if we have a $\boldsymbol{u} \in Z_h^1$, we may create a $\varphi \in Z_h^0$ which will satisfy all the boundary conditions in Z_h^0, and also $\boldsymbol{u} = \textbf{rot}(\varphi)$.

References

[1] M. Ainsworth and J.T. Oden. *A Posterori Error Estimation in Finite Element Analysis*. Wiley-Interscience, 1st edition, January 2000.

[2] I. Akkerman, Y. Bazilevs, V. M. Calo, T. J. R. Hughes, and S. Hulshoff. The role of continuity in residual-based variational multiscale modeling of turbulence. *Comput. Mech.*, 41(3):371–378, 2008.

[3] D. N. Arnold, R. S. Falk, and R. Winther. Finite element exterior calculus, homological techniques, and applications. *Acta numerica*, 15:1–155, 2006.

[4] Y. Bazilevs, V. M. Calo, T. J. R. Hughes, and Y. Zhang. Isogeometric fluid-structure interaction: theory, algorithms, and computations. *Comput. Mech.*, 43(1):3–37, 2008.

[5] Y. Bazilevs, V.M. Calo, J.A. Cottrell, J.A. Evans, T.J.R. Hughes, S. Lipton, M.A. Scott, and T.W. Sederberg. Isogeometric analysis using T-splines. *Computer Methods in Applied Mechanics and Engineering*, 199(5-8):229–263, 2010.

[6] Y. Bazilevs, L. Beirão de Veiga, J.A. Cottrell, T.J.R. Hughes, and G. Sangalli. Isogeometric analysis: approximation, stability and error estimates for h-refined meshes. *Mathematical Models and Methods in Applied Sciences*, 16:1031–1090, 2006.

[7] Y. Bazilevs, C. Michler, V. M. Calo, and T. J. R. Hughes. Isogeometric variational multiscale modeling of wall-bounded turbulent flows with weakly enforced boundary conditions on unstretched meshes. *Comput. Methods Appl. Mech. Engrg.*, 199(13-16):780–790, 2010.

[8] P.B. Bornemann and F. Cirak. A subdivision-based implementation of the hierarchical B-spline finite element method. *Computer Methods in Applied Mechanics and Engineering*, 2012.

[9] O. Botella and R. Peyret. Benchmark spectral results on the lid-driven cavity flow. *Computers & Fluids*, 27(4):421–433, 1998.

[10] A. Buffa, C. de Falco, and G. Sangalli. IsoGeometric Analysis: Stable elements for the 2D Stokes equation. *International Journal for Numerical Methods in Fluids*, 65(11-12):1407–1422, 2011.

[11] A. Buffa, J. Rivas, G. Sangalli, and R. Vázquez. Isogeometric discrete differential forms in three dimensions. *SIAM J. Numer. Anal.*, 49(2):818–844, 2011.

[12] A. Buffa, G. Sangalli, and R. Vázquez. Isogeometric analysis in electromagnetics: B-splines approximation. *Comput. Methods Appl. Mech. Engrg.*, 199(17-20):1143–1152, 2010.

[13] A. Buffa, G. Sangalli, and R. Vázquez. Isogeometric methods for computational electromagnetics: B-spline and T-spline discretizations. *J. Comput. Phys.*, 257(part B):1291–1320, 2014.

[14] K. Chang, T. J. R. Hughes, and V. M. Calo. Isogeometric variational multiscale large-eddy simulation of fully-developed turbulent flow over a wavy wall. *Comput. & Fluids*, 68:94–104, 2012.

[15] T. Dokken, T. Lyche, and K.F. Pettersen. Polynomial splines over locally refined box-partitions. *Comput. Aided Geom. Des.*, 30(3):331–356, March 2013.

[16] M. R. Dörfel, B. Jüttler, and B. Simeon. Adaptive isogeometric analysis by local h-refinement with T-splines. *Computer Methods in Applied Mechanics and Engineering*, 199(5-8):264 – 275, 2010.

[17] J. A. Evans and T. J. R. Hughes. Isogeometric divergence-conforming B-splines for the Darcy-Stokes-Brinkman equations. *Math. Models Methods Appl. Sci.*, 23(4):671–741, 2013.

[18] J. A. Evans and T. J. R. Hughes. Isogeometric divergence-conforming B-splines for the steady Navier-Stokes equations. *Math. Models Methods Appl. Sci.*, 23(8):1421–1478, 2013.

[19] J. A. Evans and T. J. R. Hughes. Isogeometric divergence-conforming B-splines for the unsteady Navier-Stokes equations. *J. Comput. Phys.*, 241:141–161, 2013.

[20] J.A. Evans. *Divergence-free B-spline Discretizations for Viscous Incompressible Flows*. PhD thesis, The University of Texas at Austin, 2011.

[21] D.R. Forsey and R.H. Bartels. Hierarchical B-spline refinement. *ACM SIGGRAPH Computer Graphics*, 22(4):205–212, 1988.

[22] C. Giannelli, B. Jüttler, and H. Speleers. THB-splines: The truncated basis for hierarchical splines. *Computer Aided Geometric Design*, 29(7):485 – 498, 2012.

[23] T.J.R. Hughes, J.A. Cottrell, and Y. Bazilevs. Isogeometric analysis: CAD, finite elements, NURBS, exact geometry and mesh refinement. *Computer Methods in Applied Mechanics and Engineering*, 194(39-41):4135–4195, October 2005.

[24] K. A. Johannessen, F. Remonato, and T. Kvamsdal. On the similarities and differences between classical hierarchical, truncated hierarchical and LR B-splines. *Submitted to Isogeometric Special Issue: Computer Methods in Applied Mechanics and Engineering*, 2014.

[25] K.A. Johannessen, T. Kvamsdal, and T. Dokken. Isogeometric analysis using LR B-splines. *Computer Methods in Applied Mechanics and Engineering*, 269:471–514, 2014.

[26] R. Kraft. *Adaptive und linear unabhängige Multilevel B-Splines und ihre Anwendungen*. PhD thesis, Stuttgart, 1998.

[27] M. Kumar, T. Kvamsdal, and K.A. Johannessen. Superconvergent patch recovery and a posteriori error estimation technique in adaptive isogeometric analysis. *Submitted to Computer methods in applied mechanics and engineering*, 2014.

[28] Dominik Mokriš, Bert Jüttler, and Carlotta Giannelli. On the completeness of hierarchical tensor-product B-splines. *Journal of Computational and Applied Mathematics*, 271(0):53–70, 2014.

[29] B. Mourrain. On the dimension of spline spaces on planar T-meshes. *Math. Comp.*, 83(286):847–871, 2014.

[30] N. Nguyen-Thanh, H. Nguyen-Xuan, S. Bordas, and T. Rabczuk. Isogeometric analysis using polynomial splines over hierarchical t-meshes for two-dimensional elastic solids. *Computer Methods in Applied Mechanics and Engineering*, 200(21–22):1892–1908, 2011.

[31] K. F. Pettersen. On the dimension of multivariate spline spaces. Technical report, Sintef ICT, sep 2013.

[32] A. Ratnani and E. Sonnendrücker. An arbitrary high-order spline finite element solver for the time domain Maxwell equations. *J. Sci. Comput.*, 51(1):87–106, 2012.

[33] D. Schillinger, L. Dedé, M.A. Scott, J.A. Evans, M.J. Borden, E. Rank, and T.J.R. Hughes. An isogeometric design-through-analysis methodology based on adaptive hierarchical refinement of NURBS, immersed boundary methods, and T-spline CAD surfaces. *Computer Methods in Applied Mechanics and Engineering*, 249–252(0):116 – 150, 2012.

[34] D. Schillinger and E. Rank. An unfitted hp-adaptive finite element method based on hierarchical B-splines for interface problems of complex geometry. *Computer Methods in Applied Mechanics and Engineering*, 200(47 - 48):3358 – 3380, 2011.

[35] T.W. Sederberg, D.L. Cardon, G.T. Finnigan, N.S. North, J. Zheng, and T. Lyche. T-spline simplification and local refinement. *ACM Transactions on Graphics*, 23(3):276–283, 2004.

[36] T.W. Sederberg, J. Zheng, A. Bakenov, and A. Nasri. T-splines and T-NURCCs. *ACM Transactions on Graphics*, 22(3):477–484, 2003.

[37] C.V. Verhoosel, M.A. Scott, R. de Borst, and T.J.R. Hughes. An isogeometric approach to cohesive zone modeling. *International Journal for Numerical Methods in Engineering*, 87(1-5):336–360, 2011.

[38] C.V. Verhoosel, M.A. Scott, T.J.R. Hughes, and R. de Borst. An isogeometric analysis approach to gradient damage models. *International Journal for Numerical Methods in Engineering*, 86(1):115–134, 2011.

[39] A.V. Vuong, C. Giannelli, B. Jüttler, and B. Simeon. A hierarchical approach to adaptive local refinement in isogeometric analysis. *Computer Methods in Applied Mechanics and Engineering*, 200(49-52):3554–3567, 2011.